A hybrid lattice Boltzmann - Navier-Stokes method on overset grids

Alexandre Suss, Ivan Mary, Thomas Le Garrec, Simon Marié

A hybrid lattice Boltzmann - Navier-Stokes method on overset grids

Alexandre Suss*, Ivan Mary†, Thomas Le Garrec‡
DAAA, ONERA, Université Paris Saclay, F-92322 Châtillon - France

Simon Marié§
Laboratoire DynFluid, F-75013 Paris - France

This paper presents an overset grid strategy in the context of a hybrid lattice Boltzmann - Navier-Stokes method for unsteady aerodynamic and aeroacoustic applications. While the overset grid approach is usually used to couple multiple overlapping grids with different mesh topologies together through interpolations, it is proposed to extend this methodology by enabling to switch between numerical methods across the grids making up the computational domain. Thereby, one can reach nearly optimal running conditions in terms of meshing strategy and numerical properties for the simulation of high Reynolds number flows. The key feature of this work lies in the way the information exchange is performed at the interface between the lattice Boltzmann method (applied on Cartesian grids) and the finite-volume Navier-Stokes method (dedicated to curvilinear meshes). All the numerical aspects of the coupling procedure are thoroughly discussed and the developed strategy is assessed on unsteady test cases representative of aerodynamic and aeroacoustic problems.

I. Introduction

Since its introduction in the 1960s, Computational Fluid Dynamics (CFD) has risen to prominence in the design process of the aerospace industry. Over the years, one of the major difficulties of CFD has been to efficiently, accurately and reliably predict turbulent flows. Indeed, most of the practical flows targeted by industrials involve turbulence whose effects strongly impact drag predictions or the noise radiated by aircraft. This led to the development of the Reynolds Averaged Navier–Stokes (RANS) formulation which remains the current workhorse of the aerospace industry owing to its low computational cost and high robustness [1]. However, in the context of a growing demand for greener aircraft and environment preservation, new industrial needs in aerodynamics and aeroacoustics require the prediction of three-dimensional unsteady turbulent flows around complex and detailed geometries for which the RANS approach is defective. As a consequence, the development of new CFD strategies that can efficiently produce high-fidelity flow solutions such as Large Eddy Simulations (LES) or Quasi-Direct Numerical Simulation (QDNS) is an important field of research. Three factors are instrumental in this: (1) the mesh generation process, which remains a bottleneck within the CFD workflow, (2) the need for accurate numerical methods able to capture broadband structures as encountered in turbulence or aeroacoustics, and (3) the intensive use of High-Performance Computing (HPC) resources and dedicated algorithms that take advantage of distributed architectures.

Firstly, with regard to the issue of meshing, although the use of unstructured meshes is becoming increasingly attractive owing to automated pre-processing tools, it has been shown that computation-wise, codes relying on structured meshes still enjoy unrivalled performances [2]. However, the generation of structured meshes remains very cumbersome and can take many months even for an expert on a configuration as complex as the HL-CRM [3]. As a means to reduce the mesh generation effort, overset grid methods [4–7] (also referred to as "Chimera" methods [8]) have been used for many years in the CFD community, in particular for structured grids. The underlying idea behind the overset grid approach is to decompose a complex geometry into several elementary components which are meshed via independent grids without alignment constraints. The computational domain is then defined by the union of the grids, the bonding of the meshes being ensured through overlapping zones. In this way, it is possible to reach nearly optimal grid quality (w.r.t. the physics of interest) in different regions of the computational domain. This is of great interest in the context of

*PhD Candidate, Department of Aerodynamics, Aeroelasticity and Aeroacoustics, alexandre.suss@onera.fr.
†Research Scientist, Department of Aerodynamics, Aeroelasticity and Aeroacoustics, ivan.mary@onera.fr.
‡Research Scientist, Department of Aerodynamics, Aeroelasticity and Aeroacoustics, thomas.le_garrec@onera.fr.
§Assistant Professor, Conservatoire National des Arts et Métiers, simon.marie@lecnam.net.

aeroacoustics where a body-fitted mesh is commonly used close to solid surfaces while a Cartesian background grid is employed in the far-field for the propagation of acoustic waves [9]. However, it is worth noting that the overset grid method requires communication between overlapping blocks during the calculation, usually performed by interpolation. Hence, great care must be taken in selecting the interpolation method so as not to deteriorate the accuracy of the numerical scheme and not to introduce any spurious phenomena. It is worth mentioning that this method has been successfully applied on a wide range of applications over the years [5, 10, 11] and enabled aeroacoustic computations over complex geometries [12, 13].

Secondly, and as stated above, high-fidelity flow simulations also require accurate numerical methods. Indeed, in the context of the simulation of turbulent flows, the numerical schemes shall be able to capture the smallest vortical structures (often of the order of a few mesh cells) and therefore should induce a very low numerical dissipation. The numerical requirements are all the more stringent when it comes to aeroacoustics since acoustic fluctuations are orders of magnitude weaker than aerodynamic fluctuations. Therefore, there is a growing interest in high-order methods for the computation of unsteady turbulent flows [14, 15]. However, there still are a number of challenges that hinder their application in an industrial context and the improvement in accuracy often comes at the expense of the overall computational time. This illustrates the need to develop numerical methods supported by high-performance computing considerations. On this very point, the lattice Boltzmann method (LBM) [16] has emerged as a fast and reliable alternative to conventional CFD methods. Indeed, the LBM has already demonstrated its potential for aeroacoustic computations owing to its low dissipation properties [17, 18]. In addition, the LBM also provides the advantage of having a very low computational cost by mesh point [18]. Nevertheless, the LBM appears to be less suited than classical finite-volume Navier-Stokes (NS) methods to the highly-resolved computation of vortical flows as encountered in boundary layers [18]. Its restriction to Cartesian grids also presents two major drawbacks. On one hand, this inevitably leads to a very large number of cells in the near-wall region and thus to a prohibitive computational cost when it comes to wall-resolved simulations. On the other hand, this feature also implies that the body surface is usually treated as an immersed boundary supplemented with a wall-law whose validity is still open to question for high-fidelity simulations [19]. Consequently, finite-volume Navier-Stokes methods might outperform the LBM in near-wall flow regions, benefiting from their great flexibility through the use of body-fitted anisotropic meshes or implicit time-stepping. Following this idea, a hybrid lattice Boltzmann - Navier-Stokes method has recently been proposed to perform efficient and accurate direct aerodynamic and aeroacoustic computations around complex geometries [20].

The present work aims to increase the flexibility of the hybrid lattice Boltzmann - Navier-Stokes method introduced in [20] by extending it to the case of overset grids. The idea is to apply a finite-volume Navier-Stokes method on structured body-fitted grids around obstacles (where high accuracy is usually required within the boundary layer) and to use the lattice Boltzmann method elsewhere on Cartesian grids so as to efficiently propagate acoustic waves or wakes. Two key elements have to be taken into account in the development of such a computational strategy. One is to put in place a precise and efficient communication protocol between the different grids and the other is to ensure a smooth transition between the lattice Boltzmann and finite-volume Navier-Stokes methods. Both aspects will be detailed in the present paper. The paper is organised as follows. In Section II, the numerical methods are introduced. Then, in Section III the overset grid methodology is presented and a thorough analysis of the interpolation methods is performed. While section IV details the extension of the hybrid lattice Boltzmann - Navier-Stokes method to overset grids, the proposed approach is validated in Section V. Finally, the capabilities of this new computational strategy are demonstrated in the case of the aeroacoustic study of the flow past a circular cylinder in Section VI.

II. Numerical framework

The hybrid lattice Boltzmann - Navier-Stokes overset grid methodology is developed in the framework of ONERA's Cassiopée/FAST CFD environment [21–23] implementing HPC dedicated solvers for unsteady fluid dynamics applications as well as pre- and post-processing functions.

A. FastS: a multiblock structured finite-volume Navier-Stokes solver

The three-dimensional compressible Navier-Stokes (NS) equations are solved using the finite-volume method on structured grids. Starting from the conservative form of the Navier-Stokes equations:

$$\frac{\partial}{\partial t}\mathbf{U} + \boldsymbol{\nabla}\cdot\mathbf{F}(\mathbf{U}) - \boldsymbol{\nabla}\cdot\mathbf{F}^{\nu}(\mathbf{U}) = \mathbf{0}, \tag{1}$$

where $\mathbf{U} = (\rho, \rho u_i, \rho E)^t$, $\mathbf{F}(\mathbf{U})$ and $\mathbf{F}^v(\mathbf{U})$ are the flow variable vector, the inviscid and viscous fluxes, respectively; the cell-centred finite volume method is obtained by splitting the computational domain Ω into N non-overlapping cells Ω_{ijk}. The integration of equation (1) over every cell of the mesh leads to a semi-discrete form as:

$$\frac{\mathrm{d}}{\mathrm{d}t}\mathbf{U}_{ijk} + \frac{1}{|\Omega_{ijk}|}\mathbf{R}_{ijk}(\mathbf{U}) = \mathbf{0}, \tag{2}$$

where $\mathbf{U}_{ijk}$ is now the mean flow variable vector evaluated at the center of Ω_{ijk}, $|\Omega_{ijk}|$ the volume of Ω_{ijk} and $\mathbf{R}_{ijk}$ the residual of the discretised convective and viscous terms.

In the present work, the convective fluxes are being approximated with a second-order accurate scheme proposed by Mary & Sagaut [24]. It relies on a hybrid centred/decentered modification of the AUSM+(P) scheme offering a good trade-off between robustness, accuracy, and computational cost. The viscous fluxes are discretised by a second-order accurate centered scheme. The time integration is carried out by means of an explicit 3^{rd}-order accurate low-storage Runge-Kutta scheme [25] or by means of an implicit 2^{nd}-order accurate backward scheme of Gear with local Newton sub-iterations [26]. All these methods have been extensively used and validated for both academic and industrial unsteady flow simulations such as a transitional separation bubble [27], airfoils in near stall configurations [24, 28] and laminar transonic buffet [29].

One major feature of the FastS flow solver is its computational efficiency since it enables to update over one complete time step up to 3.5 million cells per second and per core on a single Intel Broadwell processor [18, 30].

B. FastLBM: a multiblock structured lattice Boltzmann solver

Unlike standard CFD solvers, the LBM is based on the Boltzmann equation which describes fluids on a mesoscopic scale. Therefore, the quantities of interest are no longer macroscopic quantities (such as density and momentum) but probability distribution functions $f_i(\boldsymbol{x}, t)$. These represent the probability of finding fictive particles at position $\boldsymbol{x}$ with a given discrete velocity $\boldsymbol{\xi}_i$ at time t. The mesoscopic and macroscopic scales can be linked by taking the moments of the distribution functions, thereby recovering the variables usually used to describe fluid flows:

$$\rho(\boldsymbol{x}, t) = \sum_i f_i(\boldsymbol{x}, t) \quad \text{and} \quad \rho\boldsymbol{u}(\boldsymbol{x}, t) = \sum_i \boldsymbol{\xi}_i f_i(\boldsymbol{x}, t). \tag{3}$$

In absence of a body-force term, their evolution is given by the so-called "stream and collide" algorithm :

$$f_i(\boldsymbol{x} + \boldsymbol{\xi}_i\Delta t, t + \Delta t) = f_i(\boldsymbol{x}, t) + \Delta t\Omega_i(\boldsymbol{x}, t), \tag{4}$$

where $\Omega_i(x, t)$ denotes the collision operator. The left-hand side of Equation (4) corresponds to the streaming step along the directions of the lattice. In the present study, the D3Q19 lattice is used (see Fig. 1) meaning that the particle distribution functions are only allowed to travel along 19 directions in the three dimensions of space. Needless to say, restricting the infinite velocity space to 19 discrete velocities has an impact on the macroscopic equations recovered by the lattice Boltzmann method. Indeed, this leads to an athermal flow hypothesis (i.e. $T = T_0$) as well as a cubic Mach error term in the momentum equations thereby limiting the application of standard lattice-Boltzmann methods to weakly compressible and low Mach number flows [31].

To ensure the stability of the LBM for high Reynolds number flows, a Hybrid Recursive Regularized (HRR) collision scheme is used [32]. In this context, the collision operator reads as:

$$\Omega_i(\boldsymbol{x}, t) = f_i^{eq}(\boldsymbol{x}, t) + \left(1 - \frac{1}{\overline{\tau}}\right) f_i^{(1)}(\boldsymbol{x}, t) + \frac{1}{2}\Psi_i(\boldsymbol{x}, t). \tag{5}$$

In Equation (5), f_i^{eq} is the equilibrium distribution function, $f_i^{(1)}$ the regularised off-equilibrium one, Ψ_i a cubic Mach correction terms [33] and $\overline{\tau}$ is the discrete relaxation time of the collision model. Both the equilibrium and the regularised off-equilibrium distribution functions are expanded using the Hermite formalism:

$$f_i^{eq} = w_i \sum_{n=0}^{N} \frac{1}{c_s^{2n} n!} \boldsymbol{a}_0^{(n)} : \boldsymbol{\mathcal{H}}_i^{(n)} \quad \text{and} \quad f_i^{(1)} = w_i \sum_{n=2}^{N_r} \frac{1}{c_s^{2n} n!} \boldsymbol{a}_1^{(n)} : \boldsymbol{\mathcal{H}}_i^{(n)}, \tag{6}$$

where ":" stands for the full contraction of indices of two n^{th}-order tensors: the Hermite coefficients $\boldsymbol{a}_0^{(n)}$ and $\boldsymbol{a}_1^{(n)}$, and the discrete Hermite polynomials $\boldsymbol{\mathcal{H}}_i^{(n)} = \boldsymbol{\mathcal{H}}^{(n)}(\boldsymbol{\xi}_i)$. For more details, the interested reader is referred to [32, 34].

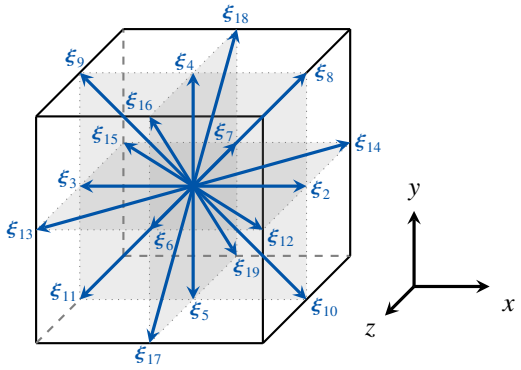

$$c_s = \frac{1}{\sqrt{3}}$$

i	1	$[\![2;7]\!]$	$[\![8;19]\!]$
$\boldsymbol{\xi}_i$	(0,0,0)	$(\pm1,0,0)$ $(0,\pm1,0)$ $(0,0,\pm1)$	$(\pm1,\pm1,0)$ $(\pm1,0,\pm1)$ $(0,\pm1,\pm1)$
w_i	1/3	1/18	1/36

Fig. 1 D3Q19 velocity set. The cube, drawn in solid lines, has an edge length of $2\Delta x$. For the sake of clarity, the rest velocity $\boldsymbol{\xi}_1 = \mathbf{0}$ is not represented as it lies at the centre of the cube. Note that each discrete velocity is expressed in its non-dimensional form. c_s is called the lattice constant.

The very essence of the HRR collision operator lies in the way the second-order off-equilibrium Hermite coefficient $\boldsymbol{a}_1^{(2)}$ is computed [32]. In the HRR framework, this tensor is hybridised. It is decomposed into a linear combination of a projected regularised part and a finite difference part, yielding:

$$\boldsymbol{a}_1^{(2)} = \sigma \left[\sum_{i=1}^{19} \boldsymbol{\mathcal{H}}_i^{(2)} \left(f_i - f_i^{eq} + \frac{\psi_i}{2} \right) \right] + (1-\sigma) \left[-\rho \overline{\tau} c_s^2 \left(\boldsymbol{\nabla u} + (\boldsymbol{\nabla u})^t \right) \right] \quad \text{with } 0 \leq \sigma \leq 1. \tag{7}$$

The spatial derivatives of the velocity field present in Equation (7) are evaluated with second-order centred finite differences. σ is a user-tuned parameter to control the amount of hyper-viscosity added to the model [32]. In the remainder of this paper, the value $\sigma = 0.995$ is adopted since this specific value of σ allows to obtain stable computations while limiting the numerical dissipation of shear and acoustic waves to a very small extent.

By construction, the streaming step of the lattice Boltzmann algorithm (4) imposes a coupling between the grid and time steps. Usually, the time step is computed following the acoustic scaling (i.e. imposed by the speed of sound c_0). Consequently, the time step Δt and the viscosity ν are then given by:

$$\Delta t = \frac{c_s \Delta x}{c_0} \quad \text{and} \quad \nu = c_0^2 \left(\overline{\tau} - \frac{1}{2} \right). \tag{8}$$

Based on these parameters, the LBM recovers the athermal and low-compressible Navier-Stokes dynamics with second-order accuracy in both space and time [35].

The FastLBM lattice Boltzmann flow solver has been optimised to take advantage of HPC ressources and is shown to be able to update up to 10 million cells per second and per core on a single Intel Broadwell processor [18].

III. Overset grid methodology

Having introduced the numerical methods used in the present work, this section focuses on the main features of the overset grid methodology. As mentioned in the introduction, this methodology consists in computing the flow field on several overlapping grids that communicate with each other through interpolations in the overlap region. In the following, the algorithm used to generate the composite grid will not be further detailed as it has already been the subject of dedicated communications [21, 36, 37]. However, the interpolation technique, which aims to ensure the continuity of the solution across meshes is thorougly discussed. Indeed, the communication between the different grids is a decisive element for the successful achievement of high-fidelity simulations.

A. General methodology

Without a loss in comprehension or generality, the overset grid methodology is described for two overlapping grids in one space dimension (see Fig. 2). Two regular grids denoted by $\mathcal{M}$ and $\mathcal{M}'$ having the same grid spacing Δx and

offset by a parameter $\eta \in [0, 1]$ (set to $\eta = 0.5$ in Fig. 2) are considerd. In most cases, the overset technique relies on a two-way communication procedure. Consequently, the main flow variables are transferred from $\mathcal{M}$ to $\mathcal{M}'$ as well as from $\mathcal{M}'$ to $\mathcal{M}$. The communication is performed through halo exchange: each grid is extended with halo regions (or ghost-cells) to apply the same numerical scheme throughout the computational domain. The number of ghost-cells is therefore fixed by the stencil of the numerical method. In the present case, even though the LBM requires only one layer of ghost-cells, all grids are extended by two layers of ghost-cells owing to the five-point stencil of the finite volume method. The flow solution in the ghost-cells is then interpolated from the overlapping grid Before diving into the details of the interpolation process, it is important to introduce some terminology related to the overset grid method. The mesh points (which actually correspond to the centre of the mesh cells in Fig. 2) can be classified as [5]:

- **receiver points** (○ and ○). The flow variables at these points are interpolated from their values in the *donor* grid. The receiver points correspond (in most of the cases) to the ghost points of each grid.
- **interior points** (○, ● and ○, ●). The flow variables at these points are computed by the corresponding numerical method (LB or FV-NS in the present case). These points are further distinguished by their role in the communication process:
  - **donor points** (○ and ○). These points are involved in the communication process: the flow variables at these points are used to compute their interpolated value at the corresponding reciever point. The number of donor points depends on the stencil of the considered interpolation method.
  - **unaffected points** (● and ●). These points are not involved in the communication process: the same numerical scheme applies as if no overset grid method was used.

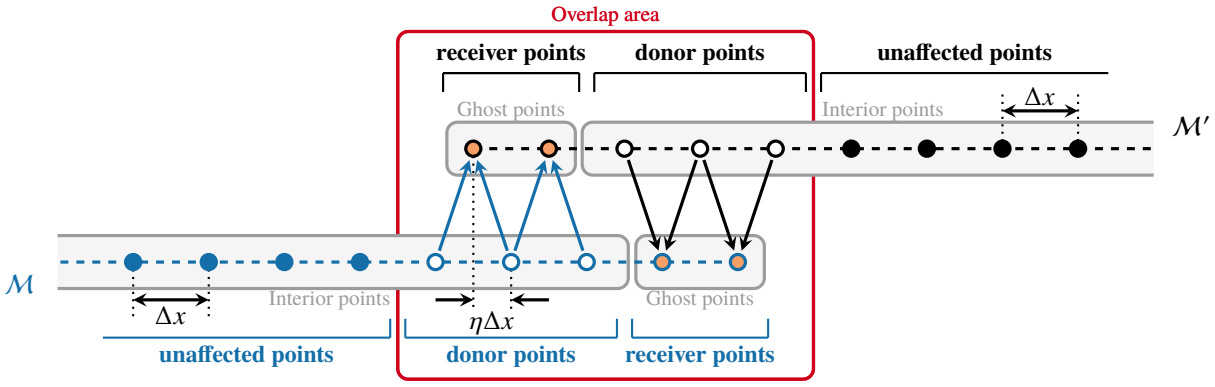

Fig. 2 1-D example of two overlapping grids with a 2nd-order centered interpolation scheme.

The area between the first receiver point of $\mathcal{M}'$ and the last receiver point of the $\mathcal{M}$ is called the overlap area. In this area, two flow solutions coexist, each defined on a different grid which leads to an increase in computational time compared to a single-grid case. Therefore, the size of the area should be as limited as possible. Yet, the distinction between donor and receiver points imposes a minimal overlap which is determined by the stencil of the interpolation scheme. Such an approach is referred to as explicit interpolation. In contrast, it is also possible to define an implicit interpolation where donor points can also be receiver points thereby reducing the overlapping area. However, implicit interpolation techniques turn out to be particularly expensive and not conducive to implementation on parallel computers [38]. Therefore, only explicit interpolations are used in the following.

B. Analysis of interpolation schemes

The issue of choosing an appropriate interpolation operator for aerodynamic and aeroacoustic applications is now addressed. While many interpolation operators can be used such as Lagrange interpolators, Hermite interpolators, B-splines [39, 40], the choice of one specific interpolation method is often based on a tradeoff between cost and accuracy. In the present work, only Lagrange interpolation schemes are studied since they are simple to implement and inexpensive (w.r.t other interpolation methods) [39]. In addition to these two points, the selection of an appropriate interpolation scheme can also be guided by a number of other requirements.

Firstly, Chessire and Henshaw [38] recommend the use of an interpolation method that is at least of the same order as the numerical scheme used to compute the flow field on the interior points. Thus, for aerodynamic applications, linear interpolation (of order 2) may be sufficient. However, a study by Delfs [41] was able to show that linear interpolation

is not sufficient to correctly propagate acoustic waves from a curvilinear grid to a Cartesian background mesh. This suggests that high-order interpolations may be required for aeroacoustic simulations.

Secondly, the use of interpolation can also have an effect on the overall stability of the computation. Indeed, in this context, the study of Desvigne *et al.* [42] is particularly interesting as it shows that non-centred interpolation schemes can lead to numerical instabilities. It should be recalled that in a non-centred interpolation, the interpolated point does not lie in the central interval of the interpolation stencil. Moreover, the higher the order of the non-centred interpolation, the greater the instability. In the following, 2^{nd}-, 3^{rd}-, and 5^{th}-order interpolation schemes are compared (this results from the availability of 2^{nd}-, 3^{rd}-, and 5^{th}-order schemes in the former elsA flow solver [10] for which the Cassiopee pre- and post-processing tool was initially developed). Since the last two interpolation schemes are non-centred, it is important to characterise their stability for the subsequent computations.

Finally, it is important to note that most interpolation techniques used in overset methods are non-conservative. Although conservative interpolation schemes have been proposed, their implementation is very cumbersome especially as the order of interpolation increases. Since all the flows considered here are at low Mach number and shock-free, it has been decided to use non-conservative interpolations.

1. 1D Error analysis of the Lagrange polynomial interpolation

The interpolation procedure using Lagrange polynomials is first studied in the one-dimensional case. To this end, Fig. 3 depicts a non-centred interpolation procedure. The interpolation stencil (denoted by $\mathcal{S}$) is composed by N mesh points $\{\boldsymbol{x}_0, ..., \boldsymbol{x}_{N-1}\}$ such as $\boldsymbol{x}_i = \boldsymbol{x}_0 + i\Delta x$ where Δx is the uniform grid spacing. This set of N points defines $N-1$ intervals where interpolations can be performed at any arbitrary point $\boldsymbol{x} = \boldsymbol{x}_0 + (d-1+\eta)\Delta x$ where d is the number of the corresponding interpolation cell and η is the offset. Let f be a known discrete function defined on $\mathcal{S}$, its interpolated value at a receiver point $\boldsymbol{x}$ is given by the following polynomial:

$$\tilde{f}(\boldsymbol{x}) = \sum_{j=0}^{N-1} S_j(\boldsymbol{x}) f_j, \tag{9}$$

where f_j is the value of f at point $\boldsymbol{x}_j$ and $S_j(x)$ is the j-th interpolation coefficient. In the context of Lagrange interpolation, the coefficients $S_j(x)$ are constructed as polynomials of degree $N-1$ with a value of 1 at x_j and 0 at all other stencil nodes. Therefore one has:

$$S_j(\boldsymbol{x}) = \prod_{\substack{q=0 \\ q\neq j}}^{N-1} \frac{x - x_q}{x_j - x_q}. \tag{10}$$

Following the convention introduced by Desvigne [13, 42], Lagrange interpolations are referred to as LINpd, where N is the number of points of the interpolation stencil, and d corresponds to the cell where interpolation is performed. It can also be shown that the order of accuracy of the LINpd interpolation method is N. As a result, Fig. 3 illustrates the LI5p2 fifth-order non-centred Lagrange interpolation implemented within ONERA's Cassiopee/Fast CFD environment. The aim is now to quantify the performance of this family of interpolation methods by considering their induced global error, amplification and phase shift.

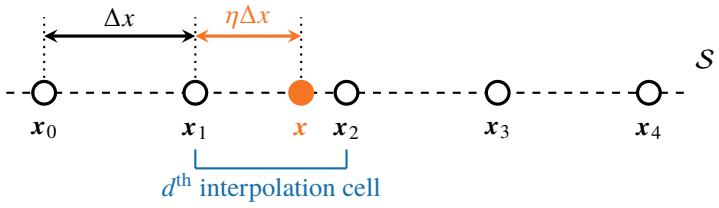

Fig. 3 1-D example of a 5^{th}-order interpolation stencil on the second cell, i.e $N = 5$ and $d = 2$.

The global interpolation error is first studied. Therefore, the function f to be interpolated is assumed to be a harmonic function of wavenumber k and phase ϕ: $f_k = e^{\mathrm{i}(kx+\phi)}$ where $\mathrm{i}^2 = -1$. The global interpolation error $\epsilon(k\Delta x)$ is defined as:

$$\epsilon(k\Delta x) = \max_{\eta\in[0,1[} \left| \frac{f_k(\boldsymbol{x}) - \tilde{f}_k(\boldsymbol{x})}{f_k(\boldsymbol{x})} \right| = \max_{\eta\in[0,1[} \left| 1 - \sum_{j=0}^{N-1} S_j e^{\mathrm{i}(d-1+\eta+j)k\Delta x} \right|. \tag{11}$$

Fig. 4a shows the global interpolation error in the wavenumber space for the 2nd-, 3rd-, and 5th-order non-centred Lagrange interpolation schemes. As expected, increasing the size of the interpolation stencil (and thus the interpolation order) reduces the interpolation error. However, the interpolation error for high wavenumbers increases significantly with the order of interpolation and can exceed 100% error for checkerboard oscillations. The source of these high error levels will subsequently be characterised in more detail. Fig. 4b and Fig. 4c also provide a closer view to the influence of the offset parameter η on the total global interpolation error in the wavenumber space. Logically, when η tends towards 0 or 1, the global interpolation error tends to 0 since the point to be interpolated coincides with a mesh point where the value of f is known exactly. In the case of the LI2p1 interpolation scheme, the result of Sherer and Scott [39], which states that the interpolation error is maximal when the point is in the middle of the interpolation cell ($\eta = 0.5$) is recovered. On the other hand in the case of non-centred schemes, the value of η_{max} for which the error ϵ reaches its maximum depends on the interpolation cell d. Indeed, if $d \leqslant \lfloor N/2 \rfloor$, then $\eta_{max} \lesssim 0.5$ (as shown in Fig. 4c) and if $d \geqslant \lceil N/2 \rceil$, then $\eta_{max} \gtrsim 0.5$.

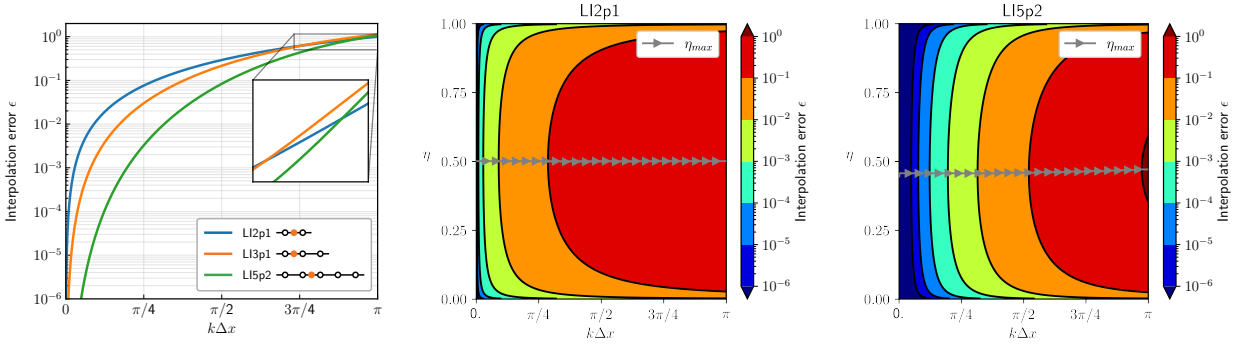

Fig. 4 Global interpolation error ϵ in the wavenumber space for the 2nd-, 3rd-, and 5th-order non-centred Lagrange interpolation schemes. (b) and (c) show the dependence of ϵ on the location of the point to be interpolated in the interpolation cell (η parameter).

In order to get more insight into the interpolation error ϵ in terms of dissipation and dispersion, the amplification and phase shift of non-centred Lagrange interpolation schemes are now quantified. The interpolation amplification α and phase shift ϕ are defined as :

$$\alpha(k\Delta x) = \max_{\eta \in [0,1[} \left| \frac{\tilde{f}_k(\boldsymbol{x})}{f_k(\boldsymbol{x})} \right| \quad \text{and} \quad \phi(k\Delta x) = \max_{\eta \in [0,1[} \arg\left(\frac{\tilde{f}_k(\boldsymbol{x})}{f_k(\boldsymbol{x})} \right). \tag{12}$$

Fig. 5a shows the amplification factor α in the wavenumber space for the 2nd-, 3rd-, and 5th-order Lagrange non-centred interpolation schemes. Surprisingly, regardless of the wavenumbers, the amplification is equal to 1, which means that the interpolation schemes do not induce any spurious amplification of the monochromatic waves. This also clarifies the source of the large error levels observed for the high wave numbers in Fig. 4a . Indeed, since no amplification is observed, the phase shift of the waves is expected to be the main cause of error in this case. Of course, if the decentering is increased (for instance with a LI5p1 interpolation), $\alpha > 1$ for high-wavenumbers which compromises its practical use as it may lead to severe instabilities. Fig. 5b depicts the phase error in the wavenumber space. Regardless of the interpolation scheme, the phase error is very small for low wavenumbers but it increases rapidly for $k\Delta x \geq \pi/4$. It should be noted that even though the phase error decreases when increasing the interpolation stencil, non-centred Lagrange interpolations have a greater phase error than the linear centered case LIp2. Hence, this explains the fact that $\epsilon > 1$ for high wavenumbers for the LI3p1 and LI5p2 interpolation schemes.

2. 2D Error analysis of the Lagrange polynomial interpolation

The interpolation procedure is now investiaged in a two-dimensional case. Indeed, although the subsequent computations are carried out on 3D domains, the mesh is set to be uniform in the transverse direction so that only 2D interpolations are used.

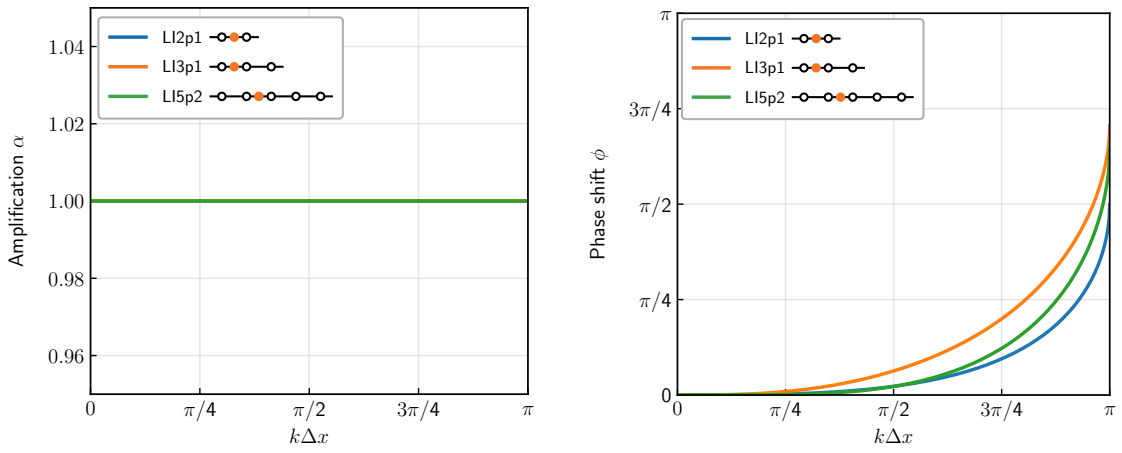

(a) **(b)**

Fig. 5 Interpolation error in terms of (a) amplification α and (b) phase-shif ϕ for the 2nd-, 3rd-, and 5th-order non-centred Lagrange interpolation schemes.

Before diving into the analysis, the implemention of two-dimensionnal interpolations should be specified. The overset grid method introduced in this work is meant to be able to handle non-coincident curvilinear and Cartesian grids. Thus, the shape of the interpolation medium is likely to vary from one grid to another and even from one point to another. In order to overcome this difficulty, the choice was made in ONERA's Cassiopeia/Fast environment to use a tensorisation of 1D interpolations. Thus, regardless of the grid topology, the interpolation stencil is mapped in a reference regular Cartesian space [40], where 1D interpolation can be applied by directions (see Fig. 6).

Since in practice all interpolations are made in the Cartesian reference domain, the theoretical framework for the analysis of 2D interpolations assumes a Cartesian domain (ξ, ζ) as shown on the right side of Fig. 6. It has recently been shown that the approximation of the mapping can have an influence on the interpolation error [43]. However, for all the computations discussed below the exact mapping will be known so that no additioanl error can arise.

The interpolation of the function f at point x is done in two steps. The first step is to horizontally interpolate the function f for the different ζ ordinates along the vertical line through x. This leads to N intermediate interpolated points (○). Secondly, the interpolation is carried out vertically along the line made up of the intermediate interpolated points. Therefore, the interpolated value of f at point x obtained by the tensor product of two 1D interpolations is given by:

$$\tilde{f}(\boldsymbol{x}) = \sum_{i=0}^{N-1} \sum_{j=0}^{N-1} S_i(\boldsymbol{x}) S_j(\boldsymbol{x}) f_{ij}, \tag{13}$$

where f_{ij} is the value of f at point $(\boldsymbol{\xi}_i, \boldsymbol{\zeta}_j)$ and $S_i(x), S_j(x)$ are the interpolation coefficients. In the context of Lagrange interpolation, the coefficients $S_j(x)$ (resp. $S_i(x)$) are constructed as polynomials of degree $N-1$ with a value of 1 at x_j (resp. x_i) and 0 at all other stencil nodes. Therefore one has:

$$S_{ij}(\boldsymbol{x}) = S_i(\boldsymbol{x}) S_j(\boldsymbol{x}) = \prod_{\substack{q=0 \\ q \neq j}}^{N-1} \frac{\boldsymbol{x} - \boldsymbol{\xi}_q}{\boldsymbol{\xi}_j - \boldsymbol{\xi}_q} \prod_{\substack{q=0 \\ q \neq j}}^{N-1} \frac{\boldsymbol{x} - \boldsymbol{\zeta}_q}{\boldsymbol{\zeta}_j - \boldsymbol{\zeta}_q}. \tag{14}$$

Following the convention introduced by Desvigne [13, 42], 2D Lagrange interpolations are referred to as LINpd $\otimes$ LINpd, where N is the size of the interpolation stencil, and d is the number of the cell where interpolation is performed. As is the 1D case, the performance of this family of interpolation methods is now quantified by considering their global interpolation error, amplification and phase shift. To this end, the function f to be interpolated is assumed to be a harmonic function of wavenumbers k_ξ, k_ζ and phase ϕ: $f_k = e^{\mathrm{i}(k_\xi \xi k_\zeta \zeta + \phi)}$ where $\mathrm{i}^2 = -1$.

Fig. 7a shows the iso-contours of the global interpolation error in the wavenumber space for the 2$^{\text{nd}}$-, 3$^{\text{rd}}$-, and 5$^{\text{th}}$-order non-centred Lagrange interpolation schemes. As already observed in the one-dimensional case, increasing

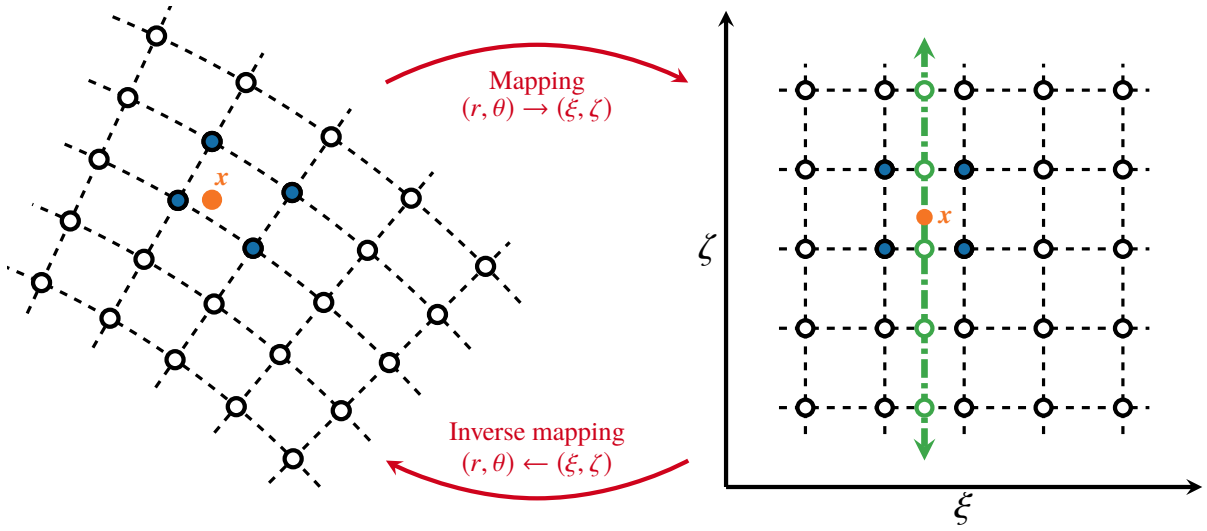

Fig. 6 2-D interpolation at a receiver point x by tensor product of 1-D fifth-order interpolations. The curvilinear grid is mapped onto a Cartesian regular grid with unit spacing. First, 5 preliminary 1-D interpolations are performed at each constant value of ζ. A final 1-D interpolation is then performed along the green arrow.

the size of the interpolation stencil (and thus the interpolation order) reduces the interpolation error, especially for low wavenumbers. However, it can now be seen that all the interpolation schemes exhibit a region where the error is greater than 100%. Moreover, the higher the order of interpolation, the larger this area is. It can also be noted that the centred interpolator LI2p1 $\otimes$ LI2p1 seems to have better isotropy than its non-centred counterparts. The global interpolation error is now broken down into amplification and phase error. Fig. 7b shows that the 2D interpolations based on the LI2p1 and LI3p1 methods preserve the non-amplification of the waves. Conversely, for the most extended stencil (LI5p2), a wide area where $\alpha > 1$ is observed although not present in a mono-dimensional case. Thus, all waves discretised by less than 4 points per wavelength are unstable for this type of interpolation. It is therefore advisable to use this interpolation in well-resolved areas or else to use an amplification control [42] or to switch to a centred interpolator. Regarding the phase shift, Fig. 7c highlights the same conclusions as in 1D. However, it can be noted that the phase error is enhanced for waves propagating at 45°. Finally, it can be concluded from this short analysis that while for the LI2p1 and LI3p1 interpolation methods the interpolation error manifests itself in the form of a phase shift, in the case of the L5p2 scheme both a phase shift and a wave amplification are responsible for the interpolation error.

C. Validation of the overset grids methodology: advection of a vortex

The overset grid methodology is first validated for full Navier-Stokes and lattice Boltzmann computations. The main purpose of this section is to highlight the differences in behaviour between these two methods in the presence of overset grids. This will allow a better understanding of the results in the context of the hybrid lattice Boltzmann - Navier-Stokes method. To this end, the case of a barotropic vortex [44] convected in a freestream is investigated. This test case is performed in the inviscid limit so as to directly investigate the numerical dissipation and the stability of the overset methodology. The initial flow field is given by:

$$\begin{cases} \rho(x,y)|_{t=0} &= \rho_0 \exp\left[-\dfrac{\epsilon^2}{2c_s^2}\exp\left(-\dfrac{(x-x_c)^2+(y-y_c)^2}{R_c^2}\right)\right], \\ u_x(x,y)|_{t=0} &= \mathrm{M}c_0 - \epsilon\left(\dfrac{y-y_c}{R_c}\right)\exp\left[-\dfrac{(x-x_c)^2+(y-y_c)^2}{2R_c^2}\right], \\ u_y(x,y)\big|_{t=0} &= \epsilon\left(\dfrac{x-x_c}{R_c}\right)\exp\left[-\dfrac{(x-x_c)^2+(y-y_c)^2}{2R_c^2}\right], \end{cases} \tag{15}$$

where $\rho_0 = 1.1765$ kg.m^{-3} is the free-stream density, c_0 is the speed of sound, $\epsilon = 0.07c_0$ is the vortex strength and $R_c = 0.1$ m is the characteristic radius of the vortex. The vortex is initially located at $(x_c, y_c) = (2.5, 2.5)$, and is

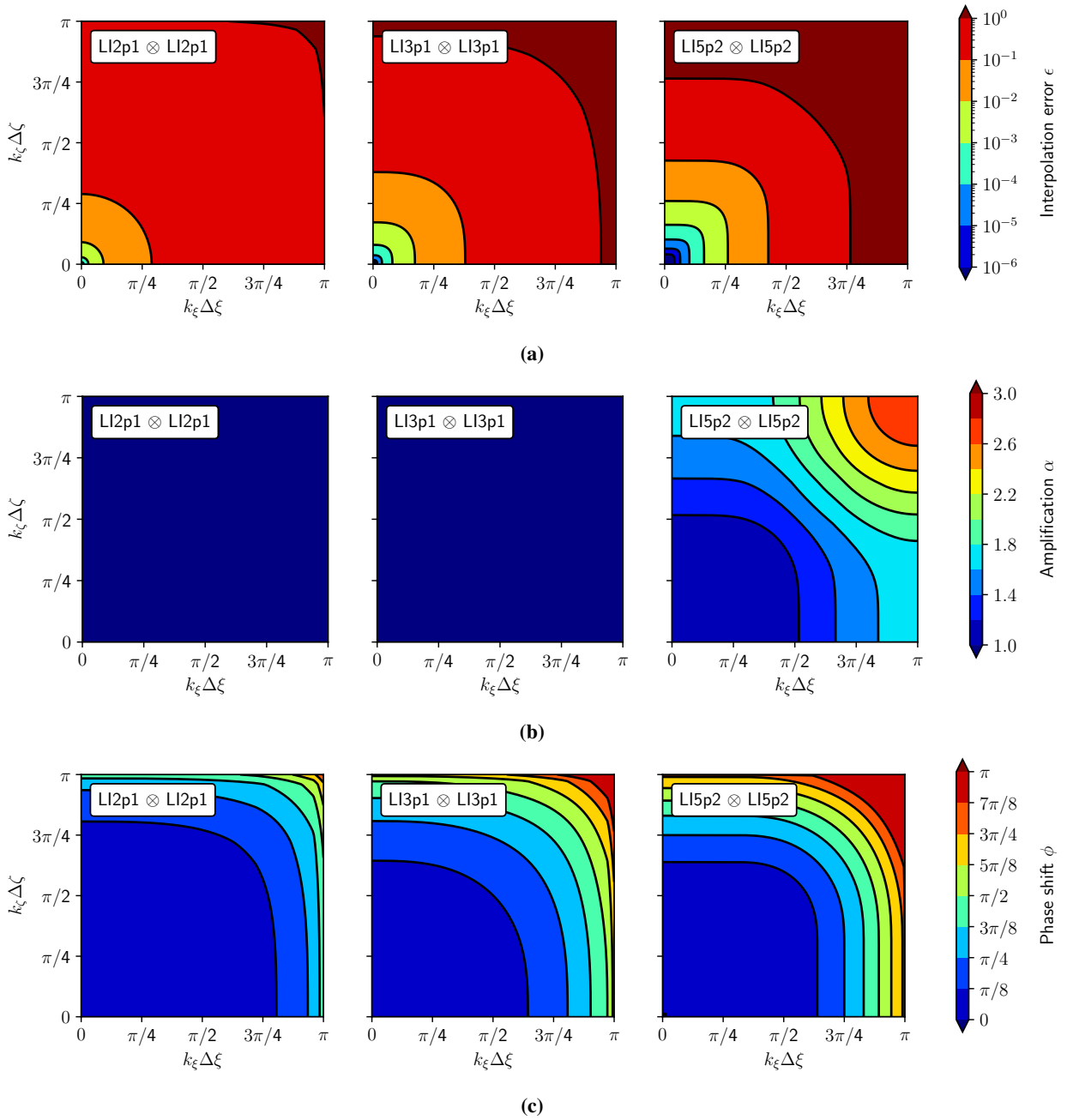

Fig. 7 Interpolation error ϵ in the two-dimensional wavenumber space obtained through the tensorisation of the 1D 2nd-, 3rd-, and 5th-order non-centred Lagrange interpolation schemes. (a) Global interpolation error ϵ, (b) amplification α and (c) phase-shift ϕ.

convected along the x direction at a Mach number of 0.1.

The computational domain consists of a pseudo-2D periodic box of size $[5L, 5L, 10\Delta x]$ with L being the reference length equal to 1 m. Two grid configurations are compared (see Fig. 8), with various grid resolutions. The first grid is a single block setup, consisting of a single Cartesian grid with a uniform cell size $\Delta x = L/n_x$ where n_x is the number of grid points per unit length. The second grid configuration relies on the overset grid method: a Cartesian block is superimposed to a background Cartesian grid. The overset block is centred on the middle domain, and shifted by half a grid step (i.e. $\eta = 0.5$ according to the notations introduced in Fig. 3). The cell size is identical in both grids.

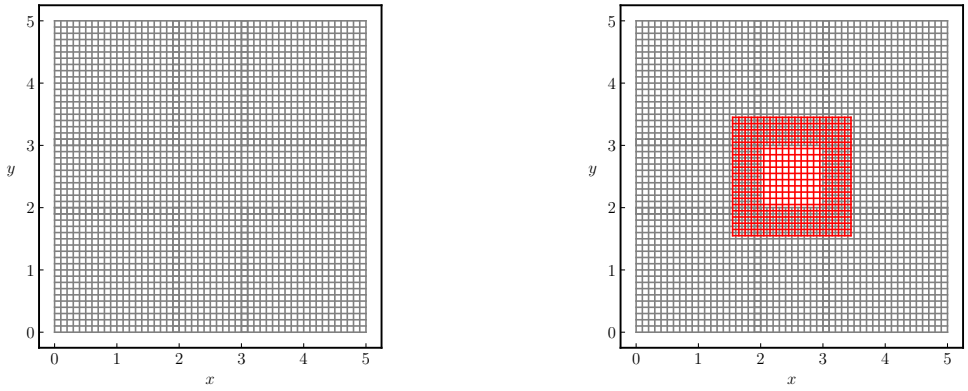

(a) Reference grid. **(b) Overset grid.**

Fig. 8 Computational domains used for the validation of the overset grid methodology. The red grid is offset by one half grid spacing in the x and y directions w.r.t. the background grid. One point out of ten is plotted.

1. Validation in the case of a full Navier-Stokes computation

The numerical behaviour of the overset grid methodology is investigated in the framework of the finite-volume Navier-Stokes solver described in Section II.A. In this case, the interpolations between the different grids is performed at each time-step on the macroscopic flow variables, i.e. the 5 components of the state vector $\mathbf{W} = (\rho, u_i, T)^t$. Two fundamental aspects of the method are studied: on the one hand, its aptitude to maintain vortical structures over long periods of time and, on the other hand, its capacity not to emit parasitic noise when the vortex passes through the overlapping zone between the two grids.

Fig. 9a displays the non-dimensional density profiles after 5 flow-through times (FTT). Note that the "Reference" solution refers to the solution obtained on the single-block uniform grid (Fig. 8a). In addition, the extent of the overset grid is shown by the grey-dashed vertical lines. First of all, it should be noted that, regardless of the interpolation order, no discontinuity in the solution is observed in the vicinity of the interface between the two grids. Focusing on the vortex depression, differences between the interpolation methods are nevertheless noticeable. Indeed, the LIp2 interpolation method (i.e. a linear interpolation) induces a slight numerical dissipation of the solution. However, by increasing the order of the interpolation (order 3 or higher), the phenomenon of numerical diffusion disappears and the solution obtained using the overset grid method is perfectly superimposed to the one obtained on the single-block uniform grid. With regard to the stability of the method, the simulation was continued up to 20 FTT and no spurious oscillation or amplification could be observed. This is mainly due to the fact that the vortex is finely resolved in this case.

In order to get more insight into the effect of the overset grid methodology on the accuracy of the computation, the simulated density field ρ is compared to its theoretical counterpart ρ_{th} (i.e. simple convection of the vortex). This is done by computing the L^2 error metric over the whole computational domain:

$$L^2(\rho) = \sqrt{\frac{1}{n_x n_y n_z} \frac{\sum_{x,y,z} |\rho(x,y,z) - \rho_{th}(x,y,z)|}{\sum_{x,y,z} \rho_{th}(x,y,z)}} \tag{16}$$

Fig. 9b shows the evolution of the L^2 error metric as a function of the grid resolution $n_x = L/\Delta x$ for the two grid configurations ("Match" refers to the single-block configuration) and various interpolation orders. By comparing the error curve of the reference computations and the one performed with the LI2p1 interpolation scheme, the remark of Chessire and Henshaw [38] makes sense: in the case of the LIp2 interpolation scheme (of lower formal order than the numerical method), it is the interpolation error that drives the convergence. By switching to a third-order interpolation (LI3p1) method or a fifth-order interpolation (LI5p2) method this problem is solved and the order of convergence of the scheme is recovered. Moreover, for a given grid resolution, the error metrics are almost identical for the single-block grid and the third- and fifth-order overset method, which indicates that the overset grid method does not introduce significant additional numerical errors.

Finally, in order to examine the emission of spurious acoustic waves, Fig. 9c presents instantaneous snapshots of the fluctuating pressure $\Delta p = p - p_{ref}$ when the vortex passes through the overlapping interface between the grids (indicated

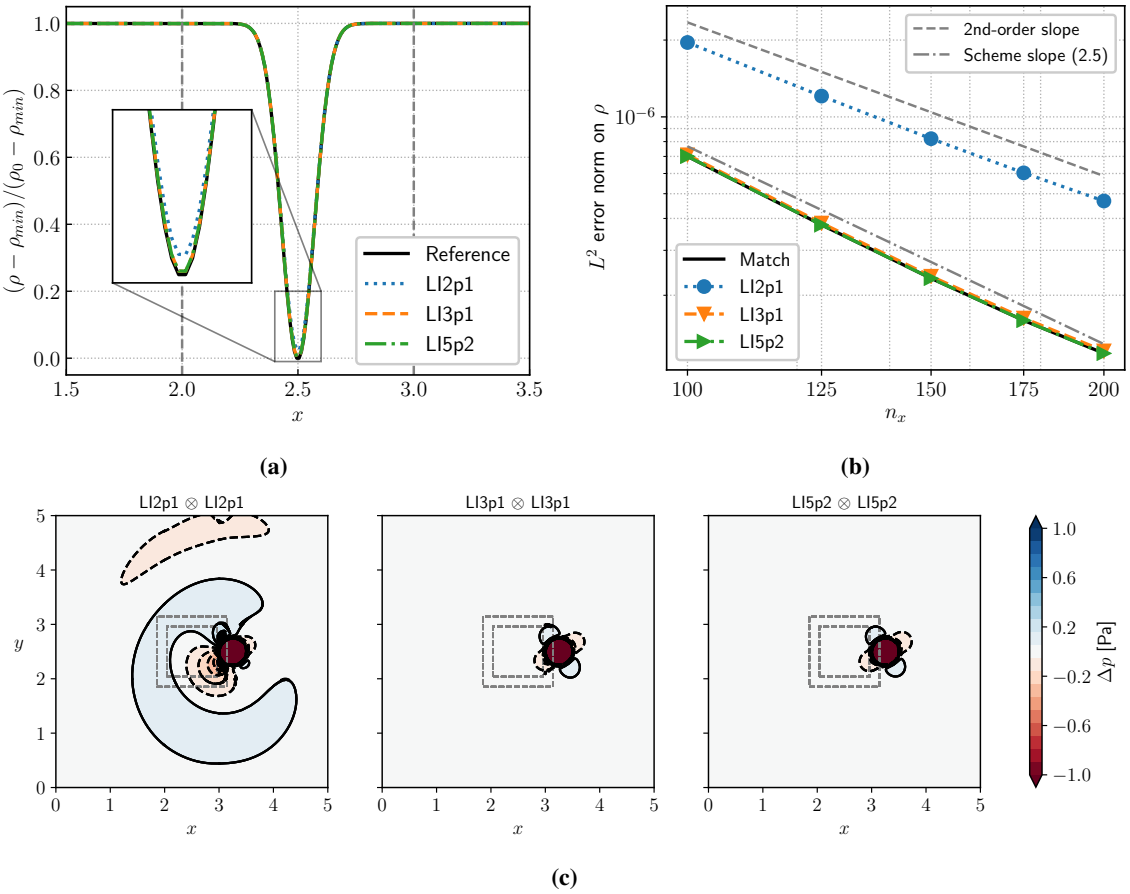

Fig. 9 Advection of a vortex on overset grids in the case of a full finite-volume Navier-Stokes computation. (a) Non-dimensional density profiles after five flow-through times, (b) Convergence rate of the overset method, and (c) Spurious acoustic waves generated by the space-interpolation method.

by the grey-dashed lines). In order not to introduce any other source of noise, characteristic boundary conditions [45] have been imposed on the edges of the computational domain. The use of second-order Lagrange interpolations leads to the generation of spurious noise. Note that for Fig. 9c, iso-contours of the fluctuating pressure Δp are within the range ± 1 Pa which represents less than 1% of the vortex depression. It can be seen, in accordance with the theoretical analysis proposed in Section III.B, that increasing the order of interpolation leads to levels of spurious noise of less than $\pm$ 1 Pa. This also validates the ability of non-centred interpolation schemes to perform aeroacoustic simulations (provided they are applied in sufficiently resolved areas).

2. Validation in the case of a full LBM computation

The same analysis as above is now carried out in the case where the overset grid methodology is applied to the lattice Boltzmann solver introduced in Section II.B. It is important to note that validating the overset grid approach with fixed meshes is rather original since in the LBM literature the overset grid method is always applied in the case of rotating grids [6, 46–48]. A major difference compared to the Navier-Stokes case arises in the quantities being transferred between the two grids. Indeed, the LBM is based on the evolution of distribution functions. Thus, the most direct approach consists in interpolating, at each iteration, the 19 distribution functions (in 3D) from one grid to another. However, this strategy is only possible if the grids are fixed. In the case of relatively moving grids, it is the moments of the distribution functions that must necessarily be interpolated, since only these have physical meaning and tensor properties [6]. More recently, some authors have proposed to combine these two approaches via a so-called "direct coupling" method [47]. In the present case, which focuses on fixed grids, the two interpolation methods (on distribution functions and on their moments) have been compared and led to the same results. Thus, in this Section, only the case of

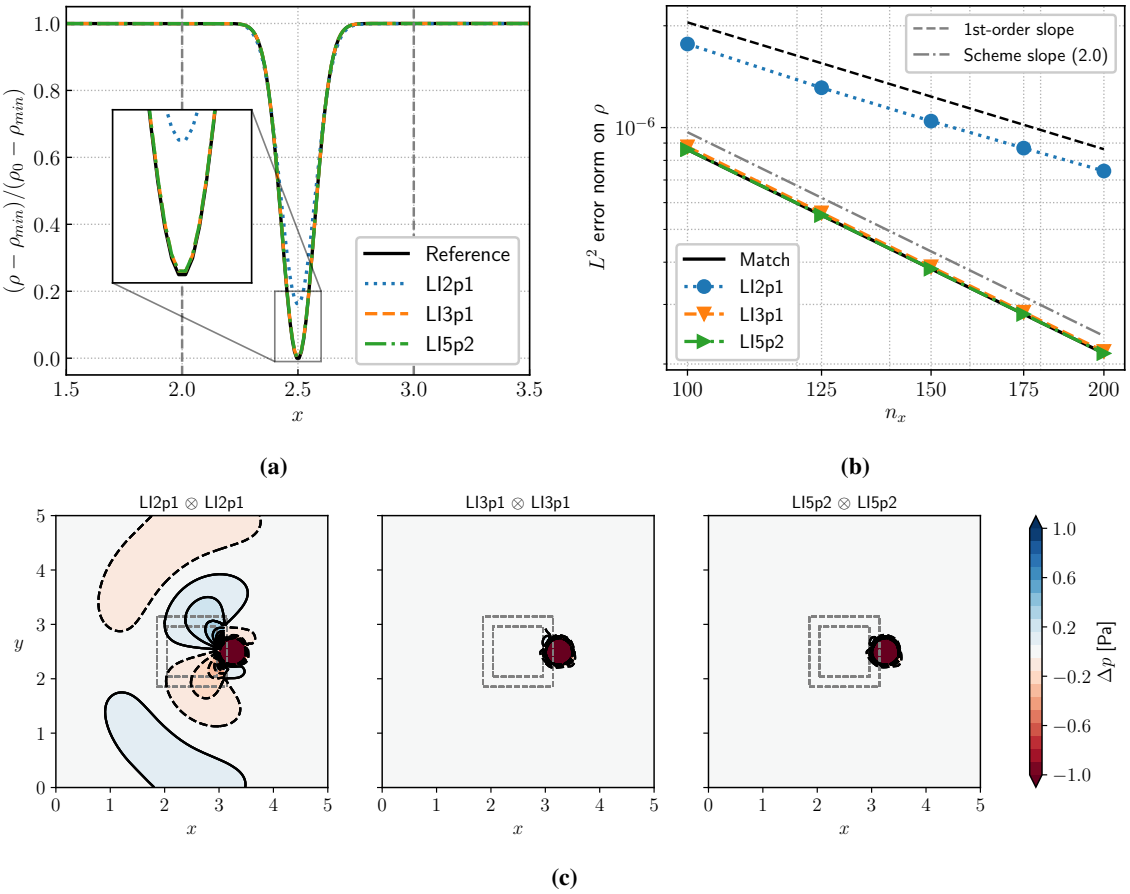

Fig. 10 Advection of a vortex on overset grids in the case of a full lattice Boltzmann computation. (a) Non-dimensional density profiles after five flow-through times, (b) Convergence rate of the overset method, and (c) Spurious acoustic waves generated by the space-interpolation method.

the direct interpolation of distribution functions will be discussed.

Fig. 10a displays the non-dimensional density profiles after 5 flow-through times (FTT). Just as for the Navier-Stokes case, no discontinuity in the density profile is observed in the vicinity of the interface between the two grids. However, notable discrepancies can be seen in the numerical dissipation induced by the overset grid method. Indeed, with the linear interpolation method (LIp2) the vortex core is strongly dissipated and to a much greater extent than in the case of the finite-volume Navier-Stokes method. This phenomenon has already been observed in the case of interpolation-supplemented lattice Boltzmann schemes [49]. Theoretical developments in [49] have shown that a linear interpolation leads to the emergence of a spurious viscous term in the momentum equations solved by the LBM that accounts for this high level of numerical dissipation. Yet, by increasing the order of the interpolation (order 3 or higher), the phenomenon of numerical diffusion disappears and the solution obtained using the overset grid method is perfectly superimposed to the one obtained on the single-block uniform grid. Similarly to the NS case, the simulation was continued up to 20 FTT and no spurious oscillation or amplification could be observed. This further proves the stability of the overset grid method with the HRR collision operator [48].

Fig. 10b shows the evolution of the L^2 density error metric as a function of the grid resolution for the lattice Boltzmann overset method. Surprisingly, one can notice that, even if the order of interpolation of the LI2p1 method coincides with the formal order of the LBM (second-order in space and time), the observed convergence is only of 1^{st}-order. This behaviour can again be explained by the theoretical study of He [49]. Indeed, the spurious viscosity term arising in the macroscopic LBM equations is such that $\nu \propto \Delta x$ under acoustic scaling (see Eq. (8)). Logically, by increasing the order of interpolation (and thus removing the spurious viscosity term), the second-order of convergence of

the LBM is recovered. Moreover, for the LI3p1 and LI5p2 interpolation schemes, the error metrics are almost identical for the single-block grid and the overset method, which indicates that the overset grid method does not introduce significant additional numerical errors.

Finally, the emission of spurious acoustic waves is investigated. Fig. 10c shows instantaneous snapshots of the fluctuating pressure $\Delta p = p - p_{ref}$ when the vortex passes through the overlapping interface between the grids at the same time-step as for the NS case. For the present acoustic computations, absorbing layers [50] have been implemented at the outer boundaries of the computational domain. Again, the second-order Lagrange interpolations lead to the generation of spurious noise. The behaviour of spurious acoustic waves with respect to the increasing interpolation order is slightly different than in the NS case. Indeed, while at the fifth order no spurious waves are visible in the range of ± 1 Pa, very slight parasitic phenomena remain when using a third-order interpolation. This can be explained by the low dissipation of the LBM, which therefore tends to be more sensitive to the precision of the interpolator. All in all, this further validates the ability to perform aeroacoustic simulations in a HRR lattice Boltzmann framework with the overset grid methodology.

IV. Extension to the hybrid lattice Boltzmann - Navier-Stokes method

Having introduced and validated the overset grid methodology in the context of segregated lattice Boltzmann and Navier-Stokes solvers, this section details the extension of the overset approach to the hybrid lattice Boltzmann - Navier-Stokes method. Indeed, the aim of the present work is to enable the seamless switch between numerical methods across the grids making up the computational domain. In the following, the key components of the hybrid lattice Boltzmann - Navier-Stokes method introduced in [20] are recalled and adapted to an overset framework.

A. General methodology

To illustrate the basic idea of the hybrid lattice Boltzmann - Navier-Stokes method, a simplified non-matching 1-D case represented on Fig. 11 is studied. The computational domain is decomposed into two sub-domains such that the finite volume method is applied on Ω_{NS} and the lattice Boltzmann method is applied on Ω_{LBM}. The coupling procedure relies on a two-way communication procedure. Consequently, the flow solution is transferred from Ω_{NS} to Ω_{LBM} (⟶) as well as from Ω_{LBM} to Ω_{NS} (⟶). As proposed in [20], the communication is performed through halo exchange: each grid is extended with halo regions (or ghost-cells) where the flow solution is imposed by the facing numerical method. To be consistent with the finite volume scheme presented in Section II.A (which is based on a five-point stencil) two layers of ghost cells are added to each sub-zone making up the computational domain.

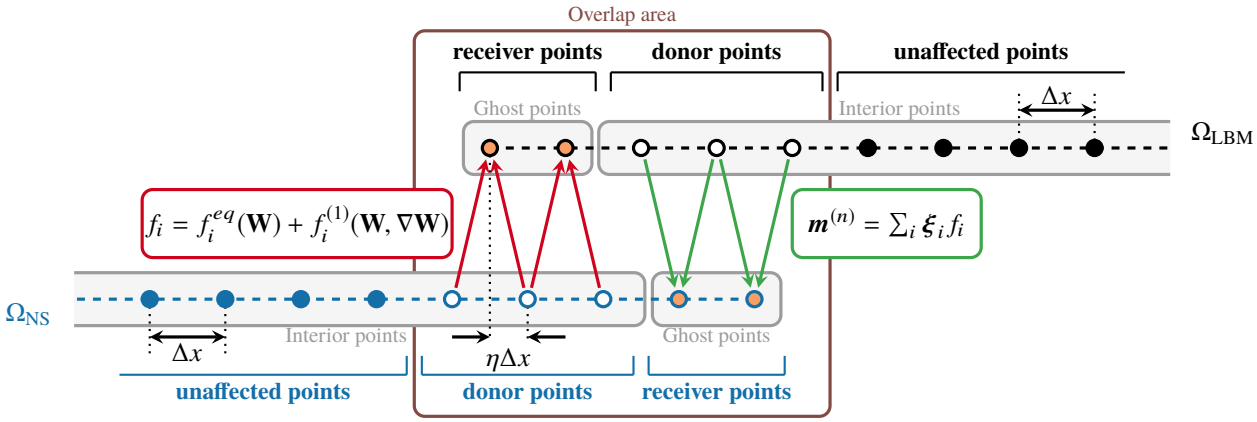

Fig. 11 1-D representation of a LB-NS coupling interface. The computational domain is decomposed into a finite-volume Navier-Stokes sub-domain and a lattice Boltzmann sub-domain.

The hybrid lattice Boltzmann - Navier-Stokes method can be broken down into 3 main components:

- **LBM to NS-FV transfer (⟶).** The information transfer from the LBM domain to the NS domain consists in imposing the flow state vector $\mathbf{W} = (\rho, u_i, T)^t$ at the NS ghost points (●). To this end, the value of the flow

state vector $\mathbf{W}$ is computed at the lattice Boltzmann donor points (●) and then interpolated onto the recieving grid. Using Equation (3), the density and velocity components of $\mathbf{W}$ are directly obtained by taking the discrete moments of the distribution functions. As discussed in [20], a rescaling step has to be performed before the exchange since the lattice Boltzmann and Navier-Stokes solvers are implemented in different systems of units. In addition, special handling must be made on the temperature. Indeed, the D3Q19 lattice employed by the LB solver only solves an athermal version of the Navier-Stokes equations and thus imposes a constant temperature $T = T_0$. As the enforcement of a uniform temperature does not allow for stable and accurate calculations, a nearly-isentropic temperature reconstruction has been proposed as [20]:

$$T(\bullet, t) = T_0 + T' = \frac{\widetilde{\rho'}(\bullet, t)(c_0^2 - RT_0)}{(\rho_0 + \widetilde{\rho'}(\bullet, t))R}, \tag{17}$$

where ρ_0 is the reference density, $\widetilde{\rho'}(\bullet, t)$ is the density fluctuation obtained through the interpolation of the LB density field, c_0 is the speed of sound and R is the gas contant.

- **NS-FV to LBM transfer (⟶).** The information transfer from the NS domain to the LBM domain is at the heart of the coupling procedure. Starting from the flow state vector $\mathbf{W}$ defined at the donor cells (○) of the FV solver, the 19 distribution functions of the D3Q19 LBM have to be imposed at the lattice Boltzmann ghost points (●). In order to alleviate this one-to-many problem, it is proposed to split the distribution functions into an equilibrium and an off-equilibrium part. While the equilibrium part can be directly computed thanks to its analytical formula [34], the off-equilibrium part is determined through a Chapman-Enskog expansion (see [20] for the detailed derivation). As a result, the off-equilibrium is shown to depend on flow state vector $\mathbf{W}$ and on its gradients. Therefore, the the 19 distribution functions in the ghost points of the LB solver are computed as:

$$f_i(\bullet, t) = f_i^{eq}(\widetilde{\mathbf{W}}(\circ, t)) + f_i^{(1)}(\widetilde{\mathbf{W}}(\circ, t), \widetilde{\nabla \mathbf{W}}(\circ, t)). \tag{18}$$

where $\widetilde{\mathbf{W}}(\circ, t)$ (resp. $\widetilde{\nabla \mathbf{W}}(\circ, t)$) is the flow state vector (resp. flow state gradient) obtained through the interpolation of its NS counterpart. It has been shown in [20] that the present mapping is intrinsically linked to advanced lattice Boltzmann regularised collision operators [32] which means the implementation of Eq. (18) does not require any additional calculations or storage.

- **Coupling of time-stepping schemes.** In the context of unsteady aerodynamic and aeroacoustic computations, the information exchanges as described above are carried out at each time step. In [20], the coupling between the LBM and explicit and implicit time advance schemes has been developed and thoroughly studied (the only restriction being that the time steps of the two methods match at the coupling interface). In particular, the explicit coupling has been proposed in the case of Runge-Kutta methods for which time interpolations are needed to ensure a smooth communication between the two solvers. In contrast, in the case of implicite time-advance schemes, the coupling is achieved via the iterative Newton process. Contrary to the matching case, the numerical tests of Section V highlight the fact that the temporal coupling plays an important role on the robustness of the hybrid method in the case of overset meshes.

B. Computation of gradients on a structured grid of arbitrary topology

As a conclusion to the previous Section, at the coupling interface between the lattice Boltzmann and the Navier-Stokes methods, only the flow state vector $\mathbf{W}$ and its gradients are interpolated and exchanged. In the original paper [20], the computation of the gradients required to the application of Eq. (18) was performed in the vicinity of the coupling interface by means of a Cartesian finite difference method. Indeed, hitherto the interface between the two numerical methods was always positioned between two Cartesian mesh blocks. As the aim of the present work is to gain flexibility from the viewpoint of meshing (by superimposing curvilinear and Cartesian grids for instance), it is necessary to extend the gradient calculation procedure initially proposed.

While the finite difference formalism could be retained by using a coordinate transformation method allowing the passage between a curvilinear physical mesh and a unitary Cartesian computational mesh [51], it is proposed to switch back to the finite-volume formalism already present in the Navier-Stokes solver. This ensures greater robustness and a lower computational cost. Thus, the gradients of the conservative variables are calculated using Green's formula on the

control volumes of the finite-volume mesh. The gradient in the x_i direction of a quantity ϕ is then obtained from:

$$\left.\frac{\partial \phi}{\partial x_i}\right|_{\Omega_c} \approx \frac{1}{|\Omega_c|}\int_{\Omega_c}\frac{\partial \phi}{\partial x_i}\,\mathrm{d}\Omega = \frac{1}{|\Omega_c|}\int_{\partial\Omega_c}\phi\cdot n_i\,\mathrm{d}\Gamma = \frac{1}{|\Omega_c|}\sum_{l=1}^{\substack{4\text{ in 2D}\\6\text{ in 3D}}}\phi|_{\Gamma_l}\cdot n_i|_{\Gamma_l}\,, \tag{19}$$

where Ω_c is a cell of the finite-volume mesh and $\boldsymbol{n}$ is the unitary outward-facing normal of face Γ_l. It is important to note that, in this framework, the gradient is assumed to have a uniform value in the cell Ω_c.

The actual procedure is detailed in Fig. 12. The calculation of the gradient, defined at the centre of each cell of the mesh, requires the knowledge of the value of the variable ϕ at the middle of each face of the control volume. These interface values are then calculated by taking the average of the values of ϕ defined in the neighbouring cells.

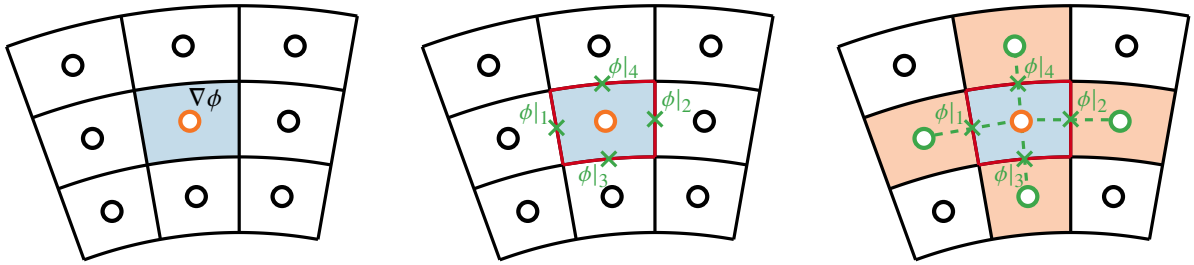

Fig. 12 Computation of gradients on a structured grid of arbitrary topology. To compute the value of $\nabla\phi$ defined the center of a mesh cell (a), an intermediate value of ϕ at the center of each face (b) is calculated by taking the average of the two nearest neighbours (c).

C. Spectral analysis of combined space and time interpolations

During the validation process of the overset grid methodology in the context of segregated lattice Boltzmann and Navier-Stokes computations, it was observed that spurious noise was generated when vortical structures passed through the overlapping area between the grids. This phenomenon can be explained with the help of signal theory tools. Indeed, Desquesnes *et al.* [52] as well as Cunha *et al.* [53] have shown that the interpolation process, which consists in reconstructing a continuous signal from a sampled signal and then resampling it on a second mesh, generates spectral aliasing, which causes the emission of spurious acoustic waves. In the particular case of the hybrid lattice Boltzmann - Navier-Stokes method on overset grids, two interpolations are performed simultaneously: one in space and the other in time. Therefore, the purpose of this section is to reproduce and extend the analysis of Desquesnes *et al.* [52] and Cunha *et al.* [53] in order to study the impact of this double interpolation on the spurious noise emission.

1. Theoretical framework

While in [52, 53] the spectral study of the interpolation is carried out in 1D, it is here extended to a two-dimensional case since the effect of the joint interpolation in space and time is intended to be characterised. To this end, an infinite mesh of $\mathbb{R}\times\mathbb{R}$ with a uniform space step Δx and a uniform time step Δt is considered so that for every point $\zeta = (x_i, t_j)$ one has $x_i = i\Delta x$ and $t_j = j\Delta t$. Hereafter, the coordinates x_i and t_j are assumed to be independent. Let f be a square-integrable function that is to be interpolated. The interpolation procedure in the case of the lattice Boltzmann - Navier-Stokes coupling can then be broken down into 5 steps as shown in Fig. 13:

- **Step 0.** The continuous function f is first discretised on the donor grid. From signal theory, the resulting discrete function (denoted hereafter by f_d) is defined as:

$$\begin{aligned} f_d(x,t) &= f(x,t)\text{Ш}_{\Delta x}\text{Ш}_{\Delta t} \\ &= \sum_{n=-\infty}^{\infty}\sum_{m=-\infty}^{\infty} f(nx,mt)\delta(x-n\Delta x)\delta(t-m\Delta t). \end{aligned} \tag{20}$$

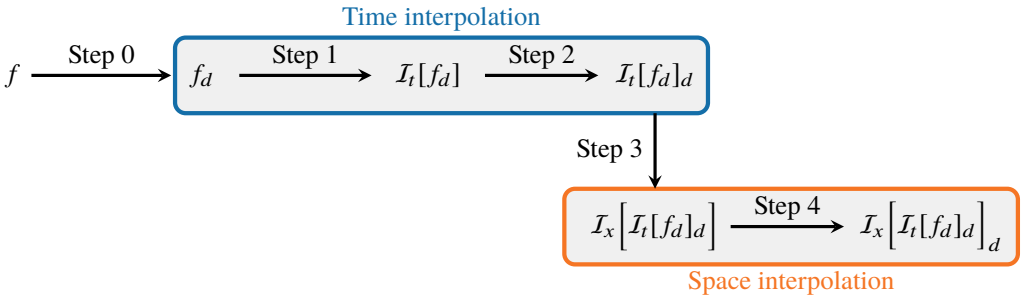

Fig. 13 Interpolation procedure for a given function f in the context of the hybrid lattice Boltzmann - Navier-Stokes method on overset grids.

In Eq. (20), the shorthand notation Ш_Δ is used to designate the Dirac comb of period Δ which is given by $\text{Ш}_\Delta(\xi) = \sum_{n\in\mathbb{Z}} \delta(\xi - n\Delta)$ where δ is the Dirac distribution. Since the focus is on the generation of spurious frequencies, the effect of each stage of the interpolation process on the spectrum of f has to be tracked. For this purpose, the Fourier transform of f_d is computed through:

$$\mathcal{F}[f_d](\alpha,\omega) = \frac{1}{\Delta x \Delta t} \sum_{m_1=-\infty}^{\infty} \sum_{m_2=-\infty}^{\infty} \mathcal{F}[f]\left(\alpha - \frac{2\pi m_1}{\Delta x}, \omega - \frac{2\pi m_2}{\Delta t}\right), \tag{21}$$

where α is the angular wavenumber and ω is the angular frequency. $\mathcal{F}[f]$ refers to the Fourier transform of the continuous function f defined by:

$$\mathcal{F}[f](\alpha,\omega) = \int_{-\infty}^{\infty}\int_{-\infty}^{\infty} f(x,t)e^{-\mathrm{i}(\alpha x+\omega t)}\mathrm{d}x\mathrm{d}t. \tag{22}$$

Herafter, the support of $\mathcal{F}[f]$ is assumed to be included in $]-\pi/\Delta x,\ \pi/\Delta x[\ \times\ ]-\pi/\Delta t,\ \pi/\Delta t[$. The discretisation process, defined by Eq. (20) induces a $(2\pi/\Delta x,\ 2\pi/\Delta t)$-periodisation of the signal. Consequently, the support of $\mathcal{F}[f_d]$ is now infinite.

- **Step 1.** The discretised function f_d is then interpolated in time. As shown in [54], interpolating a function g is equivalent to convolving this function by the associated transfer function. Thus, the resulting time-interpolated function $\mathcal{I}_t[f_d]$ reads as:

$$\mathcal{I}_t[f_d](x,t) = f_d(x,t) \star h_{\Delta t}^{\mathrm{LINpd}}(t). \tag{23}$$

In the context of Lagrange polynomial interpolation, the transfer function is directly determined by the interpolation coefficients of Eq. (10):

$$h_{\Delta}^{\mathrm{LINpd}}(\xi) = \sum_{j=1-d}^{N-d} \mathbf{1}_{[0,1[}\left(\frac{\xi}{\Delta}+j\right) S_{j+d-1}^{\mathrm{LINpd}}\left(\frac{\xi}{\Delta}+j\right). \tag{24}$$

$\mathbf{1}_{[0,1[}(x)$ is the indicator function defined as $\mathbf{1}_{[0,1[}(x) = 1$ if $x \in [0,1[$ and 0 otherwise.
Again, in order to keep track of the spectral content, the Fourier transform of the time-interpolated function $\mathcal{I}_t[f_d]$ is calculated and leads to:

$$\mathcal{F}\left[\mathcal{I}_t[f_d]\right](\alpha,\omega) = \mathcal{F}[f_d](\alpha,\omega) \times \mathcal{F}\left[h_{\Delta t}^{\mathrm{LINpd}}\right](\omega). \tag{25}$$

The analytical derivation of the Fourier transform of the transfer function associated with Lagrange interpolators is detailed in the appendix of [55].

- **Step 2.** After having interpolated in time the discrete function f_d, this new function is now sampled on a new infinite mesh of $\mathbb{R}\times\mathbb{R}$ where only the time discretisation is modified. This results in the introduction of a new time step $\Delta t'$ and an offset with respect to the first mesh denoted by η_t. Hence, for every point $\zeta = (x_i, t_j)$ one now has $x_i = i\Delta x$ and $t_j = j\Delta t' + \eta_t$. The sampling of $\mathcal{I}_t[f_d]$ reads:

$$\begin{aligned}\mathcal{I}_t[f_d]_d(x,t) &= \mathcal{I}_t[f_d](x,t)\text{Ш}_{\Delta x}\text{Ш}_{\Delta t'} \\ &= \sum_{n=-\infty}^{\infty}\sum_{m=-\infty}^{\infty} \mathcal{I}_t[f_d](nx,mt)\delta(x-n\Delta x)\delta(t-m\Delta t'),\end{aligned} \tag{26}$$

and the Fourier transform of $\mathcal{I}_t[f_d]_d$ has the following analytical expression:

$$\mathcal{F}\left[\mathcal{I}_t[f_d]_d\right](\alpha,\omega) = \frac{1}{\Delta t'}\sum_{m_3=-\infty}^{\infty} e^{-\mathrm{i}\frac{2\pi m_3}{\Delta t'}\eta_t}\mathcal{F}\left[\mathcal{I}_t[f_d]\right]\left(\alpha,\omega-\frac{2\pi m_3}{\Delta t'}\right). \tag{27}$$

Analogously to step 0, the new time discritisation defined by Eq. (26) induces a $2\pi/\Delta t'$-periodisation of the interpolated signal. Since the support of $\mathcal{I}_t[f_d]_d$ now reduces to $]-\pi/\Delta t',\ \pi/\Delta t'[$, some modes generated at step 0 and partly dissipated at step 1 are here shifted (i.e. aliased) to various frequencies. It is essential to note that this phenomenon is homogeneous in the x direction.

- **Step 3.** The discretised function $\mathcal{I}_t[f_d]_d$ is further interpolated in space. As previously, this results in the convolution of this function by the interpolation transfer function. Thus, the resulting space- and time-interpolated function $\mathcal{I}_x\left[\mathcal{I}_t[f_d]_d\right]$ reads as:

$$\mathcal{I}_x\left[\mathcal{I}_t[f_d]_d\right](x,t) = \mathcal{I}_t[f_d]_d(x,t)\star h_{\Delta x}^{\mathrm{LIN\,pd}}(x). \tag{28}$$

In the Fourier space, Eq. (28) is equivalent to:

$$\mathcal{F}\left[\mathcal{I}_x\left[\mathcal{I}_t[f_d]_d\right]\right](\alpha,\omega) = \mathcal{F}\left[\mathcal{I}_t[f_d]_d\right](\alpha,\omega)\times\mathcal{F}\left[h_{\Delta x}^{\mathrm{LIN\,pd}}\right](\alpha). \tag{29}$$

- **Step 4.** Finally, the space- and time-interpolated fuction is now sampled on a new infinite mesh of $\mathbb{R}\times\mathbb{R}$ where, this time, only the space discretisation is affected. This results in the introduction of a new space step $\Delta x'$ and an offset with respect to the first mesh denoted by η_x. As a result, for every point $\zeta = (x_i, t_j)$ one now has $x_i = i\Delta x' + \eta_x$ and $t_j = j\Delta t' + \eta_t$. The sampling of $\mathcal{I}_x\left[\mathcal{I}_t[f_d]_d\right]$ reads:

$$\begin{aligned}\mathcal{I}_x\left[\mathcal{I}_t[f_d]_d\right]_d(x,t) &= \mathcal{I}_x\left[\mathcal{I}_t[f_d]\right](x,t)\text{Ш}_{\Delta x'}\text{Ш}_{\Delta t'}\\ &= \sum_{n=-\infty}^{\infty}\sum_{m=-\infty}^{\infty}\mathcal{I}_x\left[\mathcal{I}_t[f_d]\right](nx,mt)\delta(x-n\Delta x')\delta(t-m\Delta t').\end{aligned} \tag{30}$$

All changes in the spectrum of the original function f resulting from the different interpolations in space and in time are contained in the following expression:

$$\mathcal{F}\left[\mathcal{I}_x\left[\mathcal{I}_t[f_d]_d\right]_d\right](\alpha,\omega) = \frac{1}{\Delta x'}\sum_{m_4=-\infty}^{\infty} e^{-\mathrm{i}\frac{2\pi m_4}{\Delta x'}\eta_x}\mathcal{F}\left[\mathcal{I}_x\left[\mathcal{I}_t[f_d]_d\right]\right]\left(\alpha-\frac{2\pi m_4}{\Delta x'},\omega\right). \tag{31}$$

Just as for step 0 and 3, the space discritisation defined by Eq. (30) induces a $2\pi/\Delta x'$-periodisation of the interpolated signal. Since the support of $\mathcal{I}_x\left[\mathcal{I}_t[f_d]_d\right]_d$ now reduces to $]-\pi/\Delta x',\ \pi/\Delta x'[\ \times\ ]-\pi/\Delta t',\ \pi/\Delta t'[$, some modes generated at step 0 *and* those produced at step 2 are here shifted to various frequencies. As a result, an interaction between the spurious frequencies generated through the time and space interpolations is expected to occur in the framework of the hybrid lattice Boltzmann - Navier-Stokes method on overset grids.

2. Numerical examples

In order to illustrate the aliasing phenomenon resulting from the two-fold interpolation in space and time, two numerical examples are considered. Following [52, 53], the following set of test functions is studied:

$$f_k(x,t) = \cos\left(\frac{k\pi}{16}[x-c_0(1+\mathrm{Ma})t]\right)\exp\left(-\left(\frac{x-c_0(1+\mathrm{Ma})t}{16}\right)^2\right), \tag{32}$$

where $k\in[0,14]$ is the wavenumber, c_0 is the isentropic speed of sound and $\mathrm{Ma}=0.1$ is the Mach number of the uniform flow. Each f_k is the product of a cosine and a Gaussian. Since the effect of the joint space and time interpolation is intended to be characterised, a time dependence has been added to the definition of f_k so as to mimic the propagation of an acoustic wave in a uniform flow. In the following two specific values of k are investigated namely $k=4$ and $k=10$. While the first one allows to assess the effect of the interpolations on functions exhibiting a low-frequency content (i.e. well-resolved waves), the second one is particularly interesting for understanding their impact on underresolved waves. Fig. 14 shows the space and time evolution of f_k in the case of $k=4$.

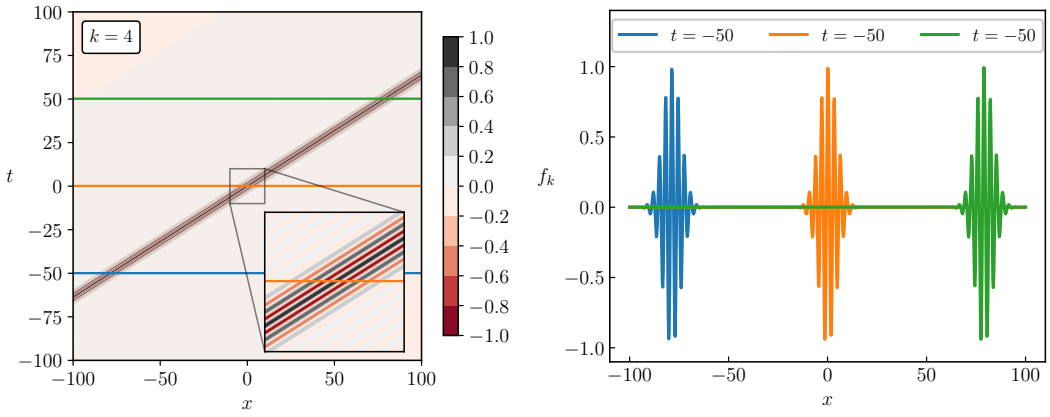

Fig. 14 Space and time evolution of f_k in the case of $k = 4$.

Fig. 15 shows the normalised Fourier transform of f_4 and f_{10}. As seen, regardless of the value of k, the Fourier transform $\mathcal{F}[f_k]$ is composed of two Gaussians centred on $\pm(k\pi/16, -k\pi/25)$ and thus, is of compact support in $]-\pi,\ \pi[$. For the sake of simplicity, the functions f_k are discretised on a uniform infinite donor grid defined by $\Delta x = 1$ and $\Delta t = 1$. All interpolations are achieved using second-order centred Lagrange polynomials (LIp2). Although these interpolation schemes are not exactly the ones used in the effective computations, they do still allow to highlight the aliasing phenomenon. The discretisation of the interpolated functions is then performed on three different receiver grids. The first one is defined by $\Delta t' = 3/4$ and $\Delta x' = 1$ (the baseline function is merely interpolated in time and not in space), the second one is defined by $\Delta t' = 1$ and $\Delta x' = 5/4$ (the baseline function is merely interpolated in space and not in time) and the third one is defined by $\Delta t' = 3/4$ and $\Delta x' = 5/4$. In all cases, the offset of the receiver grid is set to $\eta_t = \eta_x = 0$ since a non-zero offset only creates a phase shift.

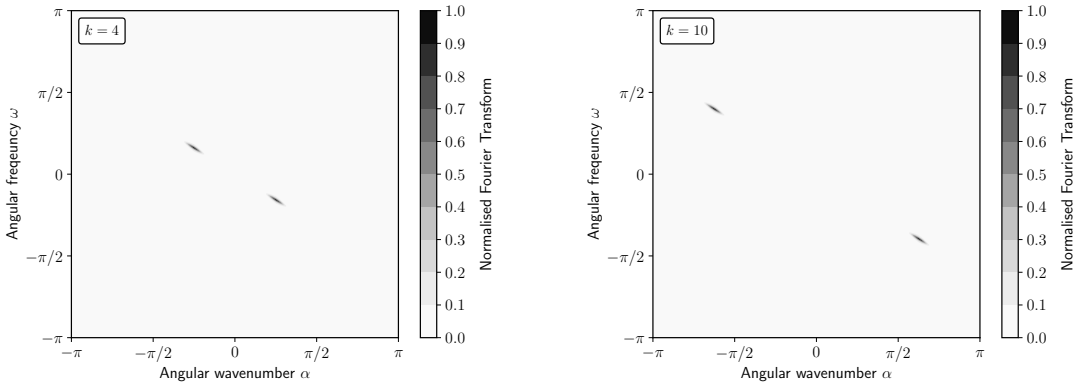

(a) **(b)**

Fig. 15 2D Normalised Fourier transform of f_k for (a) $k = 4$ and (b) $k = 10$.

Fig. 16 compares the normalised Fourier transform of the discrete function $f_{k,d}$ after the successive interpolations for $k = 4$ (Fig. 16a) and $k = 10$ (Fig. 16b) on the three receiver grids. To facilitate the analysis of the Figure, black (resp. grey) dashed lines enclose the bandwidth of the donor (resp. receiver) mesh. The first thing to note is that regardless of the wavenumber k of the test-function, the interpolation procedure does lead to the generation of spurious modes as shown in [52, 53]. If the interpolation is only performed in time, the angular wavenumber of the initial function remains unchanged: only modes with a higher angular frequency are generated. Similarly, if the interpolation is only performed in space, the angular frequency of the initial function remains unchanged: only modes with a higher angular wavenumber are generated. As such, for a low frequency base content, the amplitude of these spurious modes is very small and does not impact the solution. However, for high wave numbers (e.g. $k = 10$) the amplitude of these spurious modes can be high and lead to the generation of waves whose amplitude is very close to the one of the original signal.

The most interesting configuration is the one where interpolations are made in both space and time. Indeed, it can be observed that the pattern of the generated parasitic modes quickly becomes complex and therefore difficult to filter out. In addition, there are also new modes that emerge purely as a result of the combination of the two successive interpolations. As a result, this can be harmful in the context of aeroacoustic simulations.

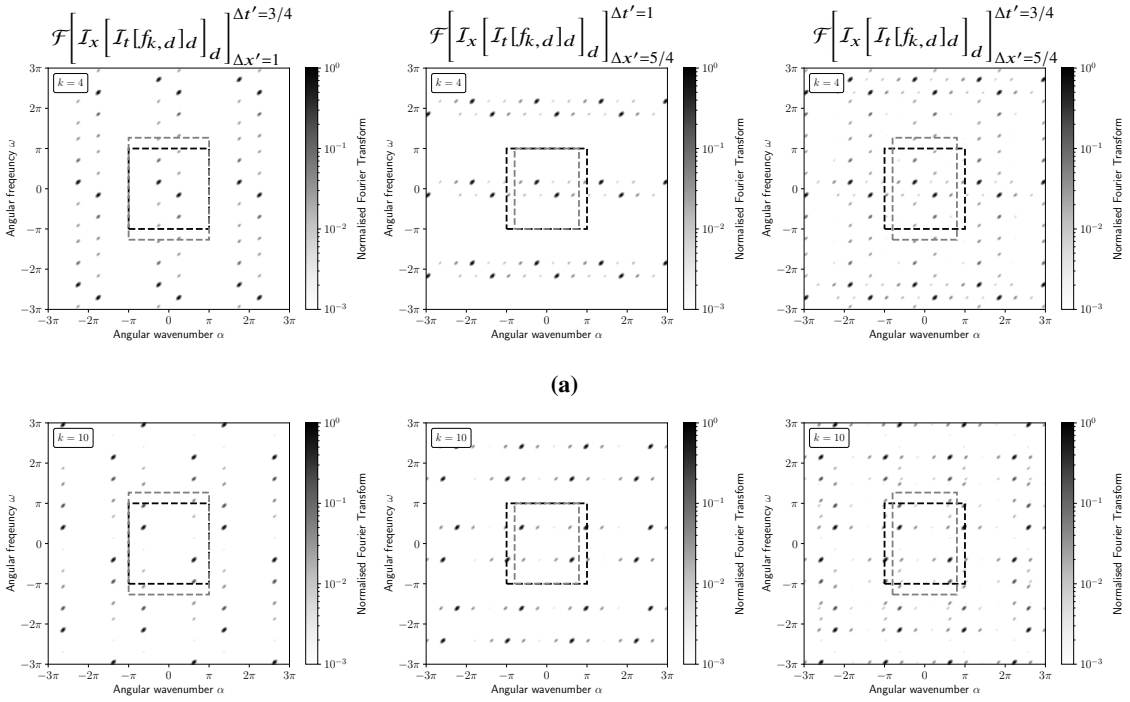

Fig. 16 2D Normalised Fourier transform of $\mathcal{I}_x\left[\mathcal{I}_t[f_{k,d}]_d\right]_d$ for (a) $k = 4$ and (b) $k = 10$ and the three receiver grids (in columns).

The theoretical analysis performed in this section has shown that the joint space and time interpolation creates spurious modes whose magnitude may, in some cases, be as large as that of the original signal. This phenomenon will further be highlighted in the subsequent Section and the interest of the time coupling of the LBM with an implicit time scheme will be shown.

V. Validation of the hybrid lattice Boltzmann - Navier-Stokes overset grid method on academic test cases

The hybrid lattice Boltzmann - Navier-Stokes overset grid methodology is now validated on two aerodynamic and aeroacoustic test cases. First, Section V.A considers a two-dimensional acoustic pulse. Then, the case of a convected vortex (already introduced in Section III.C) is investigated. Throughout this Section, a pseudo-2D periodic computational domain of size $[5L, 5L, 10\Delta x]$ with L being the reference length equal to 1 m is considered. Three different meshing strategies are compared and represented in Fig. 17. Firstly, a mesh consisting of matching Cartesian grids (see Fig. 17a) is studied and serves as a reference for the subsequent validation process. Then two overset configurations are investigated. The first (see Fig. 17b) is identical in all respects to the one already presented in Section III.C. The second one considers the overlay of a curvilinear grid on a Cartesian background mesh (see Fig. 17c). The curvilinear grid is obtained by applying the following transformation:

$$x_{\text{curvi}} = x_{\text{cart}} + 0.025 \sin\left(\frac{3\pi y_{\text{cart}}}{L}\right) \quad \text{and} \quad y_{\text{curvi}} = y_{\text{cart}} + 0.025 \sin\left(\frac{3\pi x_{\text{cart}}}{L}\right). \tag{33}$$

The lattice Boltzmann method is applied on the Cartesian background mesh while the finite-volume Navier-Stokes

method is applied on the overset grid (in red in Fig. 17). The kinematic viscosity ν is set to $\nu_{\text{air}} = 15.6 \times 10^{-6}$ m^2/s, the reference temperature is $T_0 = 300$ K and the speed of sound c_0 has a value of 347.3 m.s^{-1}. For the HRR collision operator, the hybridization parameter is $\sigma = 0.995$.

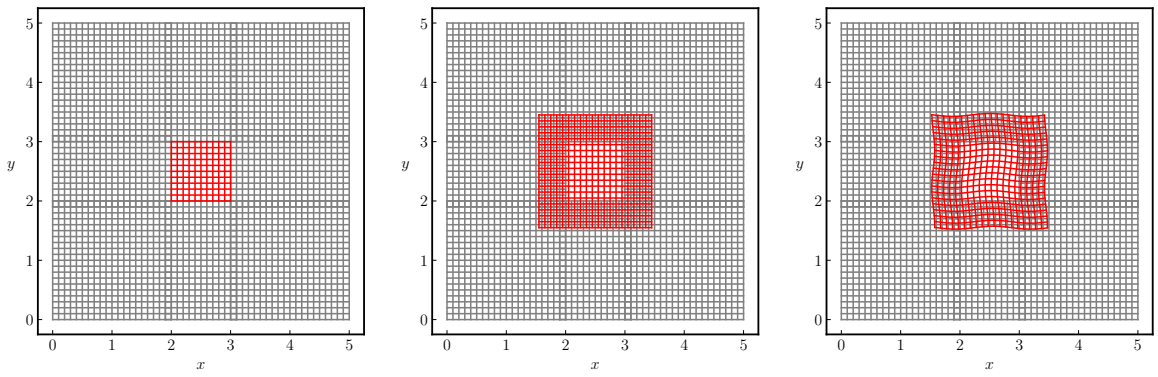

(a) Reference domain. **(b) Cartesian overset grid domain.** **(c) Curvilinear overset grid domain.**

Fig. 17 Computational domains used for the validation of the hybrid lattice Boltzmann - Navier-Stokes overset grid methodology. One point out of ten is plotted.

A. Acoustic pulse

This test case aims at assessing the aeroacoustic capabilities of the hybrid lattice Boltzmann - Navier-Stokes method with overset grids and to see whether such a method can be used for aeroacoustic simulations. In this context, the acoustic pulse is is the most standard wave propagation problem [56]. The corresponding initial flow field is given by:

$$\begin{cases} \rho(x,y)|_{t=0} &= \rho_0 \left(1 + A \exp\left(-\dfrac{[(x-x_c)^2 + (y-y_c)^2]}{2R_c^2}\right)\right), \\ \boldsymbol{u}(x,y)|_{t=0} &= \mathbf{0}, \end{cases} \tag{34}$$

where $\rho_0 = 1.1765$ kg.m^{-3} is the reference density, $A = 10^{-3}$ is the amplitude of the perturbation and $R_c = 0.1$ m its characteristic radius. The pulse is initially located at the center of the domain, i.e at $(x_c, y_c) = (2.5, 2.5)$.

The uniform grid size is set to $\Delta x = L/n_x$ where n_x is the number of grid points per unit length and the time-step is chosen so as to enforce a CFL number of $1/\sqrt{3} \approx 0.57$ for both the NS-FV and the lattice Boltzmann solvers thus ensuring a synchronous time evolution. In the following, the explicit time advance scheme will be used for the finite-volume Navier-Stokes method and only grids (a) and (b) of Fig. 17 are investigated (the results being the same in the case of the curvilinear overset grid).

Fig. 18 shows the fluctuating density profiles $\Delta\rho$ at $y = 2.5$m for various mesh resolutions and interpolation orders. The "Reference" solution corresponds to result obtained on grid (a) of Fig. 17. It can be observed from Fig. 18 that in the case of a poorly resolved wave ($n_x = 25$), the use of overlapping meshes leads to a significant generation of spurious noise which is not present in the case of conformal meshes. However, with fifth-order Lagrange interpolations, these waves are largely attenuated and the solution tends towards the reference one. The same effects are also visible in the case $n_x = 50$, even though the parasitic phenomena are much reduced. In the finely solved case ($n_x = 100$), the effect of interpolations is almost invisible whatever the considered order. It should be noted, nevertheless, that the second-order Lagrangian interpolation (i.e. linear interpolation) should be avoided in the case of aeroacoustic simulations since pseudo-stationary waves remain trapped in the overlap (as shown in the zoom boxes in Fig. 18).

In order to quantify in more detail the effect of interpolations and grid resolution on the quality of the solution in the presence of overlapping meshes, Fig. 19 plots the fluctuating density fields in the entire computational domain. While in the reference case (with matching NS and LBM grids), all the considered resolutions lead to very similar isotropic solutions, this is no longer the case when using overlapping meshes. It can be seen that the different orders of interpolation act differently on the reflected waves. Indeed, while the 2nd and 3rd order interpolators tend to emit waves at both the straight edges and the corners, the fifth-order interpolator tends to emit waves only at the corners.

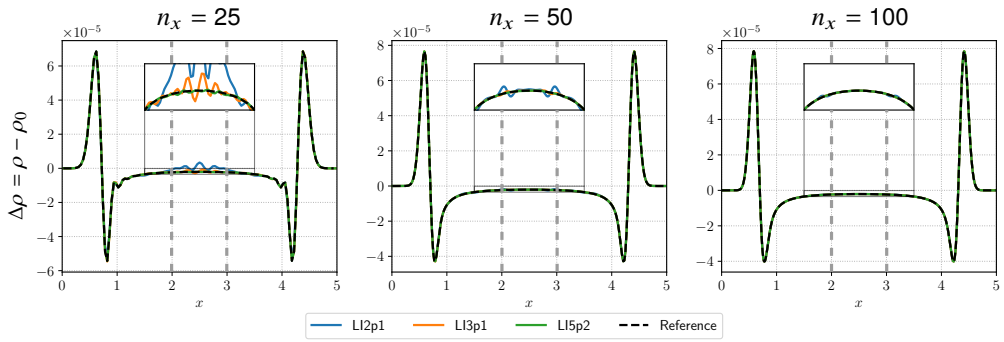

Fig. 18 Fluctuating density profiles $\Delta\rho$ at $y = 2.5$m extracted at y = 2.5m for various mesh resolution and overset interpolation orders. The grey vertical dashed lines indicate the position of the overset grid.

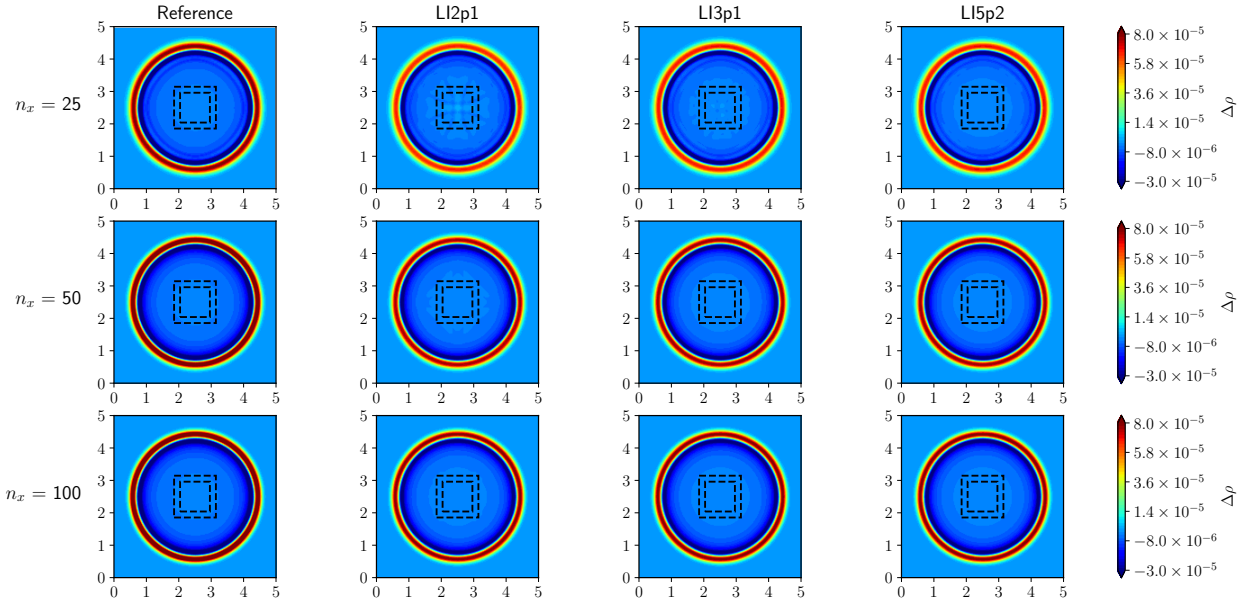

Fig. 19 Fluctuating density field $\Delta\rho$ for various mesh resolution and overset interpolation orders. The black dashed lines indicate the position of the overset grid.

This test case provides some good practices to be followed in the context of aeroacoustic simulations with the hybrid lattice Boltzmann - Navier-Stokes overset grid method. If the overlap area is in a particularly well-resolved area, then an interpolation of order three or five is sufficient to ensure the quality of the solution (order two being subject to residual acoustic waves in view of the previous discussion). Yet, if the resolution is looser, the fifth-order Lagrangian interpolation method is the only one that limits the spurious acoustic waves to an acceptable level.

B. Advection of a vortex

The case of a vortex convected across an overset grid interface is addressed here. It is a standard but very challenging test case as the frequency content if the vortex is much more broad-band than the one of the acoustic pulse. Thus, a wide range of wavelengths are excited which can interact and generate spurious phenomena. Following the case setup of Section III.C, the initial flow field is given by Eq. (15) where $\rho_0 = 1.1765$ kg.m^{-3} is the free-stream density, c_0 is the speed of sound, $\epsilon = 0.07c_0$ is the vortex strength and $R_c = 0.1$ m is the characteristic radius of the vortex. This time, the vortex is initially located at $(x_c, y_c) = (1.5, 2.5)$, and is convected along the x direction at a Mach number of 0.1 so as to investigate the effect of the overset method on the two-way exchange between the lattice Boltzmann and Navier-Stokes methods.

In the following and unless otherwise stated, the Cartesian background grid has a uniform cell size $\Delta x = L/n_x$ where $n_x = 100$ is the number of grid points per unit length. In the case of mesh (a) and (b) (see Fig. 17a), the cell size is identical in all the grids. However, for mesh (c) (see Fig. 17a), one has $\Delta x_{\text{curvi}} \in [0.9\Delta x, 1.1\Delta x]$ and $\Delta y_{\text{curvi}} \in [0.9\Delta y, 1.1\Delta y]$. The explicit time advance scheme is considered for the finite volume solver.

A qualitative validation is carried out first. To this end, Fig. 20 displays the relative density field $\rho^\star$ defined by $\rho^\star = (\rho - \rho_{\text{min},0})/(\rho_0 - \rho_{\text{min},0})$ as the vortex crosses the first overset interface (LBM to NS exchange). In order to ease the analysis, a "Reference" solution corresponding to the result obtained on the grid (a) of Fig. 17 has been added to the plot. In addition, in the case of the overset meshes, the shape of the overlaying grid is plotted with every 10th mesh point. In general, it can be observed that, regardless of the interpolation order or the overlaying grid topology, the vortex crosses the coupling interface while preserving its coherence. Once again, it can be noted that second-order interpolations should be avoided. Indeed, this leads to spurious oscillations or to a distortion of the vortex. Raising the interpolation order naturally eliminates these parasitic phenomena. However, this figure does not allow us to conclude on the interest of the fifth-order interpolation compared to the third-order since the two solutions seem identical.

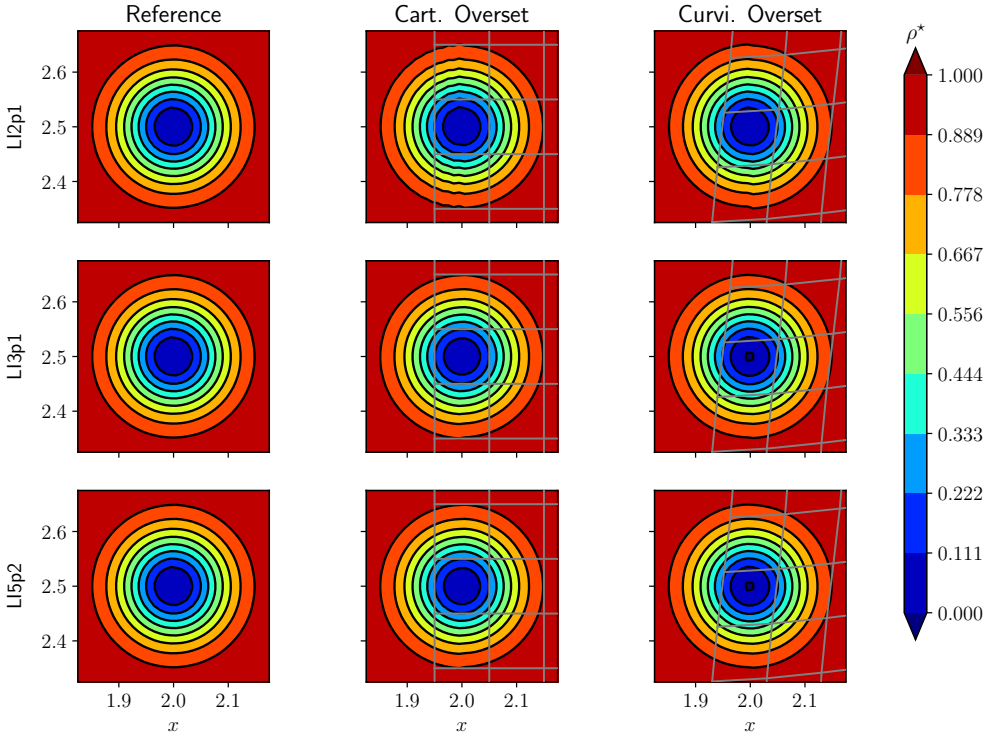

Fig. 20 Non-dimensional density field $\rho^\star = \rho^\star = (\rho - \rho_{\text{min},0})/(\rho_0 - \rho_{\text{min},0})$ as the vortex crosses the first overset interface for different grid topologies and interpolation orders. To ease the analysis of the Figure, the shape of the overlaying grid is superimposed on the density fields (one point out of ten is displayed).

In order to get more insight into the effect of the interpolation order and the overst grid topology, Fig. 21 shows the time evolution of the density profiles at $y = 2.5$m as the vortex crosses the coupling and overset interfaces. The first thing to note is that, regardless of the interpolation order, the curves corresponding to a Cartesian or a curvilinear overlaying grid are superimposed at all times. This validates the fact that the present strategy can be used on all types of grids. In the case of a centered linear interpolation (LI2p1), a slight numerical dissipation is observed but in a lesser extent than for a full LBM computation. It can therefore be concluded that the hybrid lattice Boltzmann - Navier-Stokes method exploits the advantages of both methods, since the superimposition of a NS grid onto the Cartesian LBM background grid limits the overall dissipation of the vortical structure. By increasing the order of the interpolation scheme, one recovers the behavior of the reference computation. Indeed, the results obtained with both the LI3p1 and LI5p2 interpolation scheme are in good agreement with the reference solution. Again, there is no difference in the quality of the solution between these two interpolation methods. This confirms the fact that aerodynamic simulations are

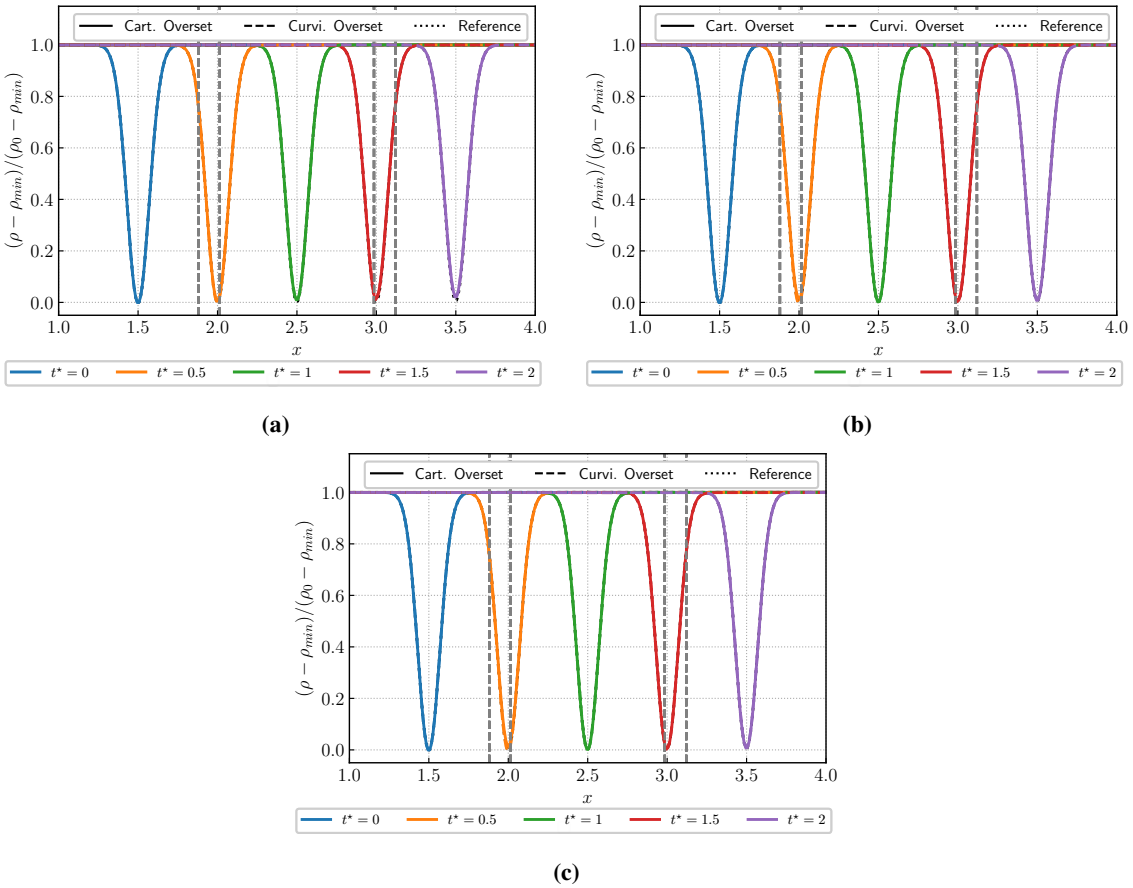

Fig. 21 Non-dimensional relative density profiles at $y = 2.5$m as the vortex crosses the coupling and overset interfaces. The gray vertical dasehd lines indicate the position of the interfaces. (a) LI2p1 Lagrange interpolation scheme, (b) LI3p1 Lagrange interpolation scheme, and (c) LI5p2 Lagrange interpolation scheme.

less demanding than aeroacoustic computations: here, a third-order interpolation scheme seems sufficient to preserve the aerodynamic quantities.

The effect of the overset grid methodology on the convergence order of the hybrid lattice Boltzmann - Navier-Stokes method is now discussed. Fig. 22 shows the evolution of the L^2 density error norm as a function of the mesh resolution $n_x = L/\Delta x$. In contrast to the pure LBM and pure NS computations, the second-order interpolation does not degrade the overall order of the method (which is of order two as shown in [20]). It can therefore be seen that despite the fact that most of the points are updated via the LBM, the use of an overset NS grid avoids the introduction of a spurious viscosity and thus preserves the order of the method. It should be noted, however, that the second-order interpolation induces a much higher level of error than a hybrid lattice Boltzmann - Navier-Stokes computation without overlapping grids. Only the third- and fifth-order interpolations allow the error levels to be approximately the same as the reference case. Fig. 22 also allows to rule on the interest of the 5th-order interpolation method. Indeed, even if on the previous figures no notable difference could be observed, the 5th-order interpolation is more precise than its 3rd-order counterpart. This can therefore be of particular interest for aeroacoustic computations.

To conclude the analysis of the convected vortex test case, it is proposed to focus on the generation of parasitic acoustics during the passage of the vortex structure at the interface between the overlapping grids. For this purpose, the periodic boundary conditions imposed until now at the outer boundaries of the computational domain are replaced by absorbing layers [50]. For the sake of clarity, only the case of mesh (b) is presented. The fifth-order interpolation scheme is used for the communication between the overset grids and a third-order time interpolation is employed between the lattice Boltzmann and Navier-Stokes solver (see [20] for further details). Fig. 23 shows the spurious noise

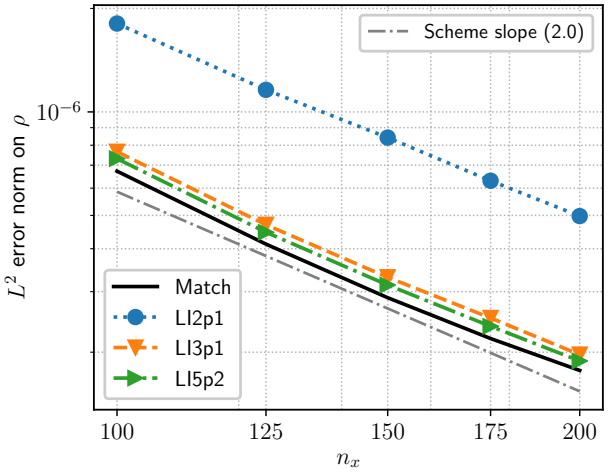

Fig. 22 Convergence rate of the hybrid lattice Boltzmann - Navier-Stokes overset method.

emission (defined as the fluctuating pressure $\Delta p = p - p_{\text{ref}}$ in Pa) when the vortex crosses the coupling and overset interface. As shown in Figure 23a, the successive application of space and time interpolation generates high-frequency spurious waves (Figure 23b zooms in on the region where these waves appear). A similar behaviour is observed if the spatial or temporal order of interpolation is changed respectively. The only way to avoid these waves is to remove the time interpolation, i.e. to switch to an implicit time advance scheme for the NS solver (as shown in Figure 23c). This result provides a further demonstration of the detrimental effects of double interpolation in aeroacoustic simulations. Moreover, as shown in Section IV.C.1, this phenomenon can be predicted by the theory a priori.

It should be noted that spurious acoustic waves are still emitted even when time interpolations are removed. These waves are inherent to the lattice Boltzmann - Navier-Stokes hybrid method and are more particularly linked to an inconsistency error between the two methods. Indeed, the LBM solves only a weakly compressible athermal version of the Navier-Stokes equations, which causes an abrupt limitation of the solution when switching to the finite volume solver which is based on the full set of compressible Navier-Stokes equations. However, as shown in [20] if the partitioning between the LBM and NS zones is done conscientiously, aeroacoustic computations are possible with this method. This is the subject of the next section.

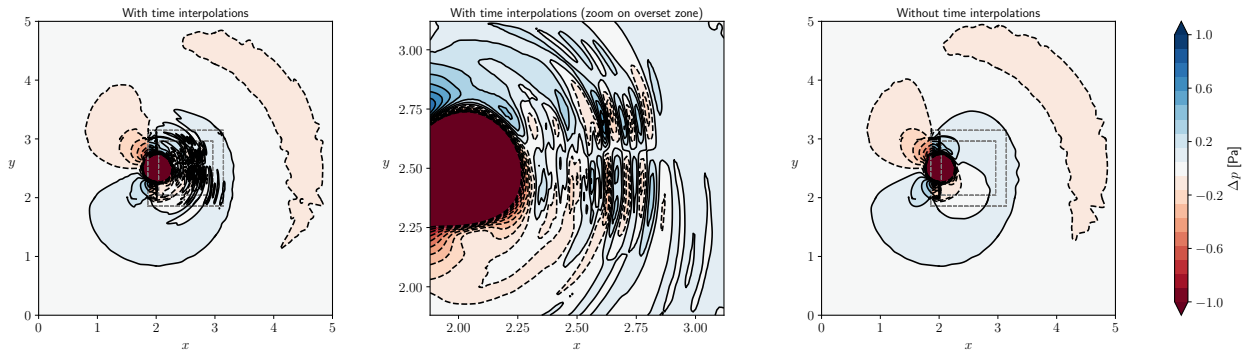

(a) **(b)** **(c)**

Fig. 23 Spurious noise emission for the convected vortex test case (a) with the LI5p2 interpolation space interpolation scheme and LI3p1 time interpolation scheme, (b) zoom on the overset grid and (c) without time interpolations (i.e. the finite-volume Navier-Stokes solver uses an implicit time scheme).

VI. Application : circular cylinder in an uniform viscous flow

As a first step towards flow simulations around complex geometries with the hybrid lattice Boltzmann - Navier-Stokes overset grid method, the sound generated by a circular cylinder in a uniform flow is investigated. Despite the simple geometry of the obstacle, the large disparity between the aerodynamic and acoustic characteristic length scales makes the direct numerical simulation of this test case a challenging task in terms of meshing and computational cost. In this context, the method proposed in this paper is of particular interest.

The same flow configuration as in Inoue and Hatakeyama [57] is considered. A cylinder of diameter $D = 1$ m is fixed in a uniform flow. The upstream Mach number M_∞ is set to $M_\infty = U_\infty/c_0 = 0.2$ and a Reynolds number $Re = U_\infty D/\nu_\infty$ of 150 is chosen in order to remain below the onset of three-dimensional fluctuations. The computational domain has a size of $[300D, 300D, 10\Delta x]$ and the cylinder is centered at its origin. Fig. 24 illustrates the flow configuration as well as the computational domain. A hybrid mesh consisting of curvilinear grid superimposed to a uniform background Cartesian grid is used. Adiabatic no-slip boundary conditions are employed on the cylinder surface and periodic boundary conditions are applied in the z direction. Non-reflecting far-field boundary conditions are also imposed at the outer boundary conditions of the computational domain. The Navier-Stokes solver (in red in Fig. 24) is applied on the body-fitted curvilinear grid in the vicinity of the cylinder while the lattice Boltzmann method is devoted to the computation of the far-field acoustics (in grey in Fig. 24). The NS domain extends throughout the wake zone since the thermodynamic closure of Eq. (17) is not applicable there.

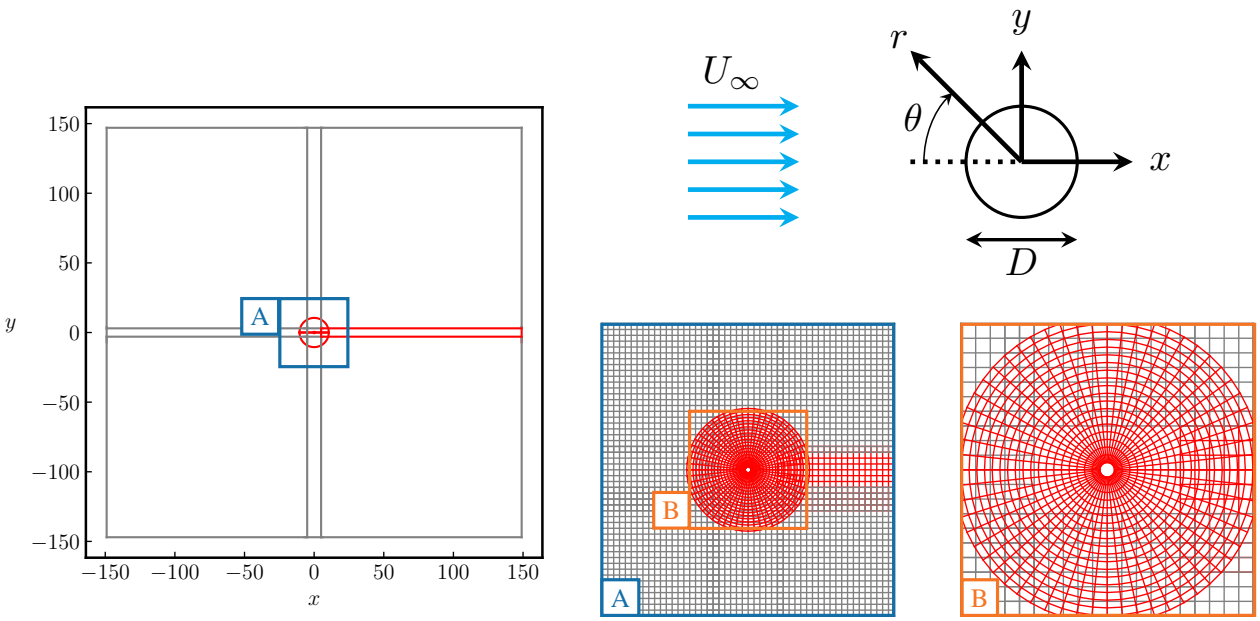

Fig. 24 Flow configuration and computational domain for the study of the flow over a circular cylinder. The grey areas are those where the LBM is applied while the red areas correspond to those where the Navier-stokes method is applied. One point out of ten is plotted.

The first points off the solid surface are placed so as to remain in the boundary layer. Consequently, on the curvilinear grid the normal grid size is taken to be $\Delta_n = \delta/10$ where δ is the boundary layer thickness and the tangent one is set to $\Delta_s = D/90$. The uniform mesh size of the backround cartesian grid is such as $\Delta x \Delta y \approx \Delta n \Delta s$ leading to $\Delta x = \Delta y = D/10$. Owing to the large disparity in grid sizes in the near- and far-fields, an implicit time-stepping is employed by the Navier-Stokes solver to ensure a physical CFL number of $1/\sqrt{3}$ at both sides of the coupling interface. In the light of previous findings, the LI5p2 spatial interpolation scheme is used for the overset communcation procedure.

First, the aerodynamic results are analysed to assess the ability of the hybrid lattice Boltzmann - Navier-Stokes overset method to accurately capture the forces acting on the cylinder. The parameters of interest are the lift and drag coefficients denoted by C_l and C_d respectively. Fig. 25 shows the time histories of the lift and drag coefficients. As readily seen from Fig. 25, the flow around the cylinder is characterised by strong oscillating aerodynamic efforts. Once

the regime is fully established, the averaged drag coefficient is $\overline{C_d} = 1.378$ showing a difference of only 0.2% with the reference simulation [57]. Similarly, the amplitude of the lift coefficient $C_l' = 0.52$ is the same as in [57]. The Strouhal number $S = Df/U_\infty$ corresponding to the non-dimensionalised frequency f of the vortex shedding is found to be equal to 0.181 showing a difference of 1% with the reference [57]. Therefore, it can be concluded that near-wall aerodynamics is well represented by the present approach.

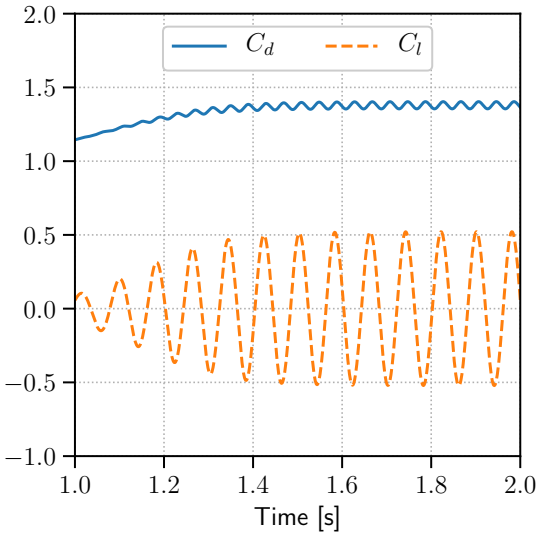

Fig. 25 Time evolution of the lift C_l and drag C_d coefficients.

The flow-induced noise is now analysed. The vortex shedding is responsible for a tonal noise at the frequency f of the vortex shedding. The corresponding pressure field is described through the fluctuating pressure field defined as $\Delta\tilde{p}(x, y, t) = \Delta p(x, y, t) - \Delta p_{\text{mean}}(x, y)$ where $\Delta p = p - p_{\text{ref}}$. Fig. 26 shows the corresponding instantaneous fluctuating pressure field $\Delta\tilde{p}$ in the whole computational domain for the hybrid lattice Boltzmann - Navier-Stokes computation. In addition, a zoom is performed at the coupling interface between the near-wall curvilinear zone (NS) and the background mesh (LBM). It can be seen that the pressure field remains continuous through the interface as no oscillations nor discontinuities in the contour lines are exhibited. The radiation pattern as well as the level of the acoustic fluctuations are in good agreement with the reference computation [57].

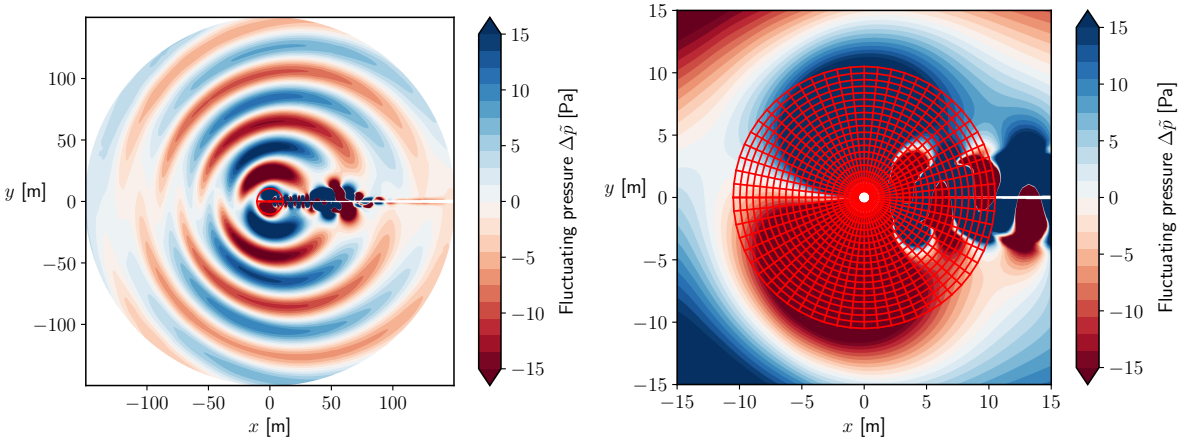

Fig. 26 Visualisation of the instantaneous fluctuating pressure field $\Delta\tilde{p}$.

In order to further validate the quality of the acoustic field computed with the hybrid lattice Boltzmann - Navier-Stokes method on overset grids, the polar plot of the root mean square fluctuating pressure defined as

$\Delta p_{\text{rms}}(x,y) = \sqrt{\overline{[\Delta p^2]}(x,y) - [\overline{\Delta p}(x,y)]^2}$ is studied. Fig. 27 shows the polar diagram of Δp_{rms} at a distance of $r = 75D$ of the cylinder. The radial length represents the magnitude on a linear scale where the outermost circle corresponds to a value of $\Delta p_{rms}/\rho_0 c_0^2 = 1 \times 10^{-4}$. The results of Fig. 27 confirm the dipolar nature of the radiated acoustic field. The directivity of the sound waves agrees with its theoretical value of $\theta_p = \pm 78.5°$ due to the Doppler effect as shown by the black dashed lines. Moreover, the directivity is superimposed to the one obtained by the reference DNS [57]. For all these reasons, the hybrid lattice Boltzmann - Navier-Stokes method on overset grids is a promising candidate for direct noise computations around complex geometries.

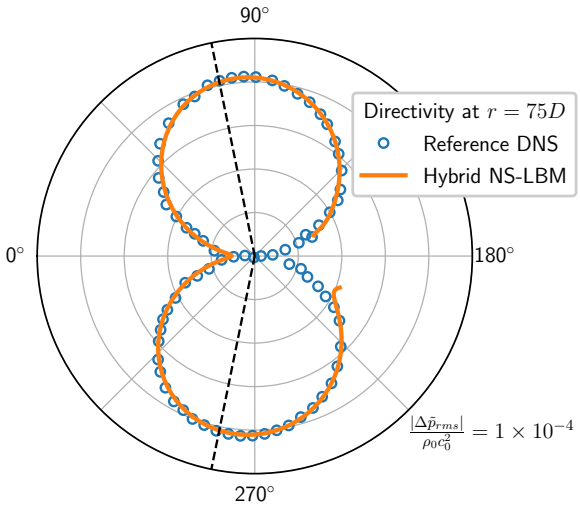

Fig. 27 Polar plots of the root mean square of the non-dimensional fluctuating pressure at a distance of $r = 75D$ of the cylinder. The symbols denote the results of the reference computation of Inoue et al. [57].

VII. Conclusion

In this present paper, a hybrid lattice Boltzmann - Navier-Stokes overset grid methodology has been proposed for the computation of unsteady fluid flow problems. As a first step, the use of non-centred Lagrange interpolations schemes to ensure the communication between overset grids has been studied and assessed in the context of segregated lattice Boltzmann and Navier-Stokes computations. Then, the coupling between the lattice Boltzmann and Navier-Stokes methods initially introduced has been described and extended to the case of overlapping grids. In this context, the aliasing phenomenon associated to the joint space and time interpolations has been derived theoretically and observed on numerical tests. Therefore it seems advisable to carry out only interpolations either in space or in time, but not both. The hybrid method is found to be able to reproduce accurately the flow physics as shown by the acoustic pulse and the convected vortex test cases. As a result, the present work helps to increase the flexibility of the hybrid lattice Boltzmann - Navier-Stokes method introduced in [20] by simplifying the mesh generation process through the use of overset grids. The finite-volume Navier-Stokes method can be applied on structured body-fitted grids around obstacles while the lattice Boltzmann method is employed on Cartesian grids so as to efficiently propagate acoustic waves or wakes. The computation of the flow and the acoustics around a circular cylinder provides a proof of this concept and paves the way toward more complex configurations. Future work will address the topic of compressible lattice Boltzmann to relax the constraint on the choice of the positioning of the coupling interface.

Acknowledgments

The authors would like to thank Stéphanie Péron and Christophe Benoit for the fruitful discussions on the overset grid methodology implemented in ONERA's Cassiopée pre- and post-processing tool.

References

[1] Schiestel, R., and Chaouat, B., "Turbulence modeling and simulation advances in CFD during the past 50 years," *Comptes Rendus - Mecanique*, Vol. 350, No. S1, 2022, pp. 1–29. https://doi.org/10.5802/CRMECA.114/.

[2] Dervieux, A., "To be structured, or unstructured, fifty years of slings and arrows," *Comptes Rendus - Mecanique*, Vol. 350, No. S1, 2022, pp. 1–6. https://doi.org/10.5802/CRMECA.115/.

[3] Ghate, A. S., Kenway, G. K., Stich, G. D., Maldonado, D., and Kiris, C. C., "A Wall-Modeled LES Perspective for the High Lift Common Research Model Using LAVA," *AIAA AVIATION 2022 Forum*, American Institute of Aeronautics and Astronautics Inc, AIAA, 2022. https://doi.org/10.2514/6.2022-3434.

[4] Chan, W. M., "Overset grid technology development at NASA Ames Research Center," *Computers and Fluids*, Vol. 38, No. 3, 2009, pp. 496–503. https://doi.org/10.1016/j.compfluid.2008.06.009.

[5] Peron, S., Benoit, C., Gleize, V., Mary, I., and Terracol, M., "A mixed overset grid/immersed boundary approach for CFD simulations of complex geometries," *54th AIAA Aerospace Sciences Meeting*, 2016. https://doi.org/10.2514/6.2016-2055.

[6] Lallemand, P., and Luo, L. S., "Lattice Boltzmann equation with Overset method for moving objects in two-dimensional flows," *Journal of Computational Physics*, Vol. 407, 2020, p. 109223. https://doi.org/10.1016/j.jcp.2019.109223.

[7] Deuse, M., and Sandberg, R. D., "Implementation of a stable high-order overset grid method for high-fidelity simulations," *Computers and Fluids*, Vol. 211, 2020, p. 104449. https://doi.org/10.1016/j.compfluid.2020.104449.

[8] Steger, J. L., Dougherty, F. C., and Benek, J. A., "A chimera grid scheme," *Advances in grid generation*, 1983.

[9] Desquesnes, G., Terracol, M., Manoha, E., and Sagaut, P., "A high order overlapping grid method for CFD/CAA coupling," *11th AIAA/CEAS Aeroacoustics Conference*, Vol. 2, 2005, pp. 914–936. https://doi.org/10.2514/6.2005-2872.

[10] Cambier, L., Heib, S., and Plot, S., "The Onera elsA CFD software: input from research and feedback from industry," *Mechanics & Industry*, Vol. 14, No. 3, 2013, pp. 159–174. https://doi.org/10.1051/MECA/2013056.

[11] Péron, S., and Benoit, C., "Automatic off-body overset adaptive Cartesian mesh method based on an octree approach," *Journal of Computational Physics*, Vol. 232, No. 1, 2013, pp. 153–173. https://doi.org/10.1016/j.jcp.2012.07.029.

[12] Deuse, M., and Sandberg, R. D., "Parametric study of multiple aerofoil self-noise sources using direct noise computation," *25th AIAA/CEAS Aeroacoustics Conference*, 2019. https://doi.org/10.2514/6.2019-2681.

[13] Desvignes, D., "Bruit rayonné par un écoulement subsonique affleurant une cavité cylindrique : caractérisation expérimentale et simulation numérique par une approche multidomaine d'ordre élevé," Ph.D. thesis, Ecole Centrale de Lyon, 2010.

[14] Ekaterinaris, J. A., "High-order accurate, low numerical diffusion methods for aerodynamics," *Progress in Aerospace Sciences*, Vol. 41, No. 3-4, 2005, pp. 192–300. https://doi.org/10.1016/J.PAEROSCI.2005.03.003.

[15] Wang, Z. J., "High-order methods for the Euler and Navier-Stokes equations on unstructured grids," *Progress in Aerospace Sciences*, Vol. 43, No. 1-3, 2007, pp. 1–41. https://doi.org/10.1016/J.PAEROSCI.2007.05.001.

[16] Krueger, T., Kusumaatmaja, H., Kuzmin, A., Shardt, O., Silva, G., and Viggen, E. M., *The Lattice Boltzmann Method: Principles and Practice*, Graduate Texts in Physics, Springer, 2016.

[17] Marié, S., Ricot, D., and Sagaut, P., "Comparison between lattice Boltzmann method and Navier-Stokes high order schemes for computational aeroacoustics," *Journal of Computational Physics*, Vol. 228, No. 4, 2009, pp. 1056–1070. https://doi.org/10.1016/j.jcp.2008.10.021.

[18] Suss, A., Mary, I., Le Garrec, T., and Marié, S., "Comprehensive comparison between the lattice Boltzmann and Navier–Stokes methods for aerodynamic and aeroacoustic applications," *Computers & Fluids*, Vol. 257, 2023, p. 105881. https://doi.org/https://doi.org/10.1016/j.compfluid.2023.105881.

[19] Piomelli, U., "Wall-layer models for large-eddy simulations," *Progress in Aerospace Sciences*, Vol. 44, No. 6, 2008, pp. 437–446. https://doi.org/10.1016/j.paerosci.2008.06.001.

[20] Suss, A., Mary, I., Le Garrec, T., and Marié, S., "A hybrid lattice Boltzmann - Navier-Stokes method for unsteady aerodynamic and aeroacoustic computations," *Journal of Computational Physics*, Vol. 485, 2023, p. 112098. https://doi.org/10.1016/J.JCP.2023.112098.

[21] Benoit, C., Péron, S., and Landier, S., "Cassiopee: A CFD pre- and post-processing tool," *Aerospace Science and Technology*, Vol. 45, 2015, pp. 272–283.

[22] http://elsa.onera.fr/Cassiopee/, 2022.

[23] https://w3.onera.fr/FAST/, 2022.

[24] Mary, I., and Sagaut, P., "Large eddy simulation of flow around an airfoil near stall," *AIAA Journal*, Vol. 40, No. 6, 2002, pp. 1139–1145.

[25] Lowery, P. S., and Reynolds, W. C., "Numerical simulation of a spatially-developping, forced, plane mixing layer," Tech. Rep. TF26, Stanford University, 1986.

[26] Daude, F., Mary, I., and Comte, P., "Self-Adaptive Newton-based iteration strategy for the LES of turbulent multi-scale flows," *Computers & Fluids*, Vol. 100, 2014, pp. 278–290.

[27] Laurent, C., "Étude d'écoulements transitionnels et hors-équilibre par des approches DNS et RANS." Ph.D. thesis, Ecole Nationale Supérieure d'Arts et Métiers, 2012.

[28] Alferez, N., Mary, I., and Lamballais, E., "Study of Stall Development Around an Airfoil by Means of High Fidelity Large Eddy Simulation," *Flow, Turbulence and Combustion*, Vol. 91, No. 3, 2013, pp. 623–641.

[29] Dandois, J., Mary, I., and Brion, V., "Large-eddy simulation of laminar transonic buffet," *Journal of Fluid Mechanics*, Vol. 850, 2018, pp. 156–178.

[30] Péron, S., Benoit, C., Renaud, T., and Mary, I., "An immersed boundary method on Cartesian adaptive grids for the simulation of compressible flows around arbitrary geometries," *Engineering with Computers*, Vol. 1, 2020, p. 3. https://doi.org/10.1007/s00366-020-00950-y.

[31] Shan, X., Yuan, X. F., and Chen, H., "Kinetic theory representation of hydrodynamics: A way beyond the Navier-Stokes equation," *Journal of Fluid Mechanics*, Vol. 550, 2006, pp. 413–441. https://doi.org/10.1017/S0022112005008153.

[32] Jacob, J., Malaspinas, O., and Sagaut, P., "A new hybrid recursive regularised Bhatnagar–Gross–Krook collision model for lattice Boltzmann method-based large eddy simulation," *Journal of Turbulence*, Vol. 19, No. 11, 2019, pp. 1051–1076.

[33] Feng, Y., Boivin, P., Jacob, J., and Sagaut, P., "Hybrid recursive regularized thermal lattice Boltzmann model for high subsonic compressible flows," *Journal of Computational Physics*, Vol. 394, 2019, pp. 82–99. https://doi.org/10.1016/j.jcp.2019.05.031.

[34] Malaspinas, O., "Increasing stability and accuracy of the lattice Boltzmann scheme: recursivity and regularization," 2015. URL http://arxiv.org/abs/1505.06900.

[35] Dellar, P. J., "An interpretation and derivation of the lattice Boltzmann method using Strang splitting," *Computers & Mathematics with Applications*, Vol. 65, No. 2, 2013, pp. 129–141. https://doi.org/10.1016/j.camwa.2011.08.047.

[36] Péron, S., "Méthode d'assemblage de maillages recouvrants autour de géométries complexes pour des simulations en aérodynamique compressible," Ph.D. thesis, École nationale supérieure d'arts et métiers, 2014.

[37] Péron, S., and Benoit, C., "A python pre-processing module for Chimera assembly," *10th Symposium on Overset Composite Grids and Solution Technology*, 2010.

[38] Chesshire, G., and Henshaw, W. D., "Composite overlapping meshes for the solution of partial differential equations," *Journal of Computational Physics*, Vol. 90, No. 1, 1990, pp. 1–64. https://doi.org/10.1016/0021-9991(90)90196-8.

[39] Sherer, S. E., and Scott, J. N., "High-order compact finite-difference methods on general overset grids," *Journal of Computational Physics*, Vol. 210, No. 2, 2005, pp. 459–496. https://doi.org/10.1016/j.jcp.2005.04.017.

[40] Guenanff, R., Sagaut, P., Manoha, E., Terracol, M., and Lewandowsky, R., "Theoretical Aspects of a Multidomain High-Order Method for CAA," *9th AIAA/CEAS Aeroacoustics Conference and Exhibit*, 2003. https://doi.org/10.2514/6.2003-3117.

[41] Delfs, J. W., "An overlapped grid technique for high resolution CAA schemes for complex geometries," *7th AIAA/CEAS Aeroacoustics Conference and Exhibit*, American Institute of Aeronautics and Astronautics Inc., 2001. https://doi.org/10.2514/6.2001-2199.

[42] Desvigne, D., Marsden, O., Bogey, C., and Bailly, C., "Development of noncentered wavenumber-based optimized interpolation schemes with amplification control for overlapping grids," *SIAM Journal on Scientific Computing*, Vol. 32, No. 4, 2010, pp. 2074–2098. https://doi.org/10.1137/090758702.

[43] Chicheportiche, J., and Gloerfelt, X., "Study of interpolation methods for high-accuracy computations on overlapping grids," *Computers & Fluids*, Vol. 68, 2012, pp. 112–133. https://doi.org/10.1016/J.COMPFLUID.2012.07.019.

[44] Wissocq, G., Boussuge, J.-F., and Sagaut, P., "Consistent vortex initialization for the athermal lattice Boltzmann method," *Physical Review E*, Vol. 101, No. 4, 2020, p. 043306. https://doi.org/10.1103/PhysRevE.101.043306.

[45] Thompson, K. W., "Time dependent boundary conditions for hyperbolic systems," *Journal of Computational Physics*, Vol. 68, No. 1, 1987, pp. 1–24. https://doi.org/10.1016/0021-9991(87)90041-6.

[46] Far, E. K., Geier, M., and Krafczyk, M., "Simulation of rotating objects in fluids with the cumulant lattice Boltzmann model on sliding meshes," *Computers and Mathematics with Applications*, Vol. 79, No. 1, 2020, pp. 3–16. https://doi.org/10.1016/j.camwa.2018.08.055.

[47] Bahlali, M. L., Yoo, H., Favier, J., and Sagaut, P., "A lattice Boltzmann direct coupling overset approach for the moving boundary problem," *Physics of Fluids*, Vol. 33, No. 5, 2021, p. 053607. https://doi.org/10.1063/5.0044994.

[48] Yoo, H., Bahlali, M. L., Favier, J., and Sagaut, P., "A hybrid recursive regularized lattice Boltzmann model with overset grids for rotating geometries," *Physics of Fluids*, Vol. 33, No. 5, 2021, p. 057113. https://doi.org/10.1063/5.0045524.

[49] He, X., "Error analysis for the interpolation-supplemented lattice-Boltzmann equation scheme," *International Journal of Modern Physics C*, Vol. 8, No. 4, 1997, pp. 737–745. https://doi.org/10.1142/s012918319700062x.

[50] Xu, H., and Sagaut, P., "Analysis of the absorbing layers for the weakly-compressible lattice Boltzmann methods," *Journal of Computational Physics*, Vol. 245, 2013, pp. 14–42. https://doi.org/10.1016/j.jcp.2013.02.051.

[51] Le Garrec, T., Gloerfelt, X., and Corre, C., "Multi-size-mesh multi-time-step algorithm for noise computation on curvilinear meshes," *International Journal for Numerical Methods in Fluids*, Vol. 74, No. 1, 2014, pp. 1–33. https://doi.org/10.1002/fld.3836.

[52] Desquesnes, G., Terracol, M., Manoha, E., and Sagaut, P., "On the use of a high order overlapping grid method for coupling in CFD/CAA," *Journal of Computational Physics*, Vol. 220, No. 1, 2006, pp. 355–382. https://doi.org/10.1016/J.JCP.2006.05.019.

[53] Cunha, G., and Redonnet, S., "On the signal degradation induced by the interpolation and the sampling rate reduction in aeroacoustics hybrid methods," *International Journal for Numerical Methods in Fluids*, Vol. 71, No. 7, 2013, pp. 910–929. https://doi.org/10.1002/FLD.3693.

[54] Schafer, R. W., and Rabiner, L. R., "A Digital Signal Processing Approach to Interpolation," *Proceedings of the IEEE*, Vol. 61, No. 6, 1973, pp. 692–702. https://doi.org/10.1109/PROC.1973.9150.

[55] Desquesnes, G., "Couplage par recouvrement de maillages curviligne/cartésien pour la simulation en aéroacoustique," Ph.D. thesis, Université Pierre et Marie Curie (Paris VI), 2007.

[56] Hardin, J. C., Ristorcelli, J. R., and Tam, C. K., "ICASE/LaRC Workshop on Benchmark Problems in Computational Aeroacoustics (CAA)," Tech. rep., NASA Technical Reports, 1995.

[57] Inoue, O., and Hatakeyama, N., "Sound generation by a two-dimensional circular cylinder in a uniform flow," *Journal of Fluid Mechanics*, Vol. 471, 2002, pp. 285–314. https://doi.org/10.1017/S0022112002002124.